

# Direct numerical simulation of gas-solid-liquid flows with capillary effects: An application to liquid bridge forces between spherical particles

Xiaosong Sun\* and Mikio Sakai†

*Resilience Engineering Research Center, School of Engineering, The University of Tokyo 7-3-1 Hongo, Bunkyo-ku, Tokyo 113-8656, Japan*

(Received 21 June 2016; revised manuscript received 22 September 2016; published 1 December 2016)

In this study, a numerical method is developed to perform the direct numerical simulation (DNS) of gas-solid-liquid flows involving capillary effects. The volume-of-fluid method employed to track the free surface and the immersed boundary method is adopted for the fluid-particle coupling in three-phase flows. This numerical method is able to fully resolve the hydrodynamic force and capillary force as well as the particle motions arising from complicated gas-solid-liquid interactions. We present its application to liquid bridges among spherical particles in this paper. By using the DNS method, we obtain the static bridge force as a function of the liquid volume, contact angle, and separation distance. The results from the DNS are compared with theoretical equations and other solutions to examine its validity and suitability for modeling capillary bridges. Particularly, the nontrivial liquid bridges formed in triangular and tetrahedral particle clusters are calculated and some preliminary results are reported. We also perform dynamic simulations of liquid bridge ruptures subject to axial stretching and particle motions driven by liquid bridge action, for which accurate predictions are obtained with respect to the critical rupture distance and the equilibrium particle position, respectively. As shown through the simulations, the strength of the present method is the ability to predict the liquid bridge problem under general conditions, from which models of liquid bridge actions may be constructed without limitations. Therefore, it is believed that this DNS method can be a useful tool to improve the understanding and modeling of liquid bridges formed in complex gas-solid-liquid flows.

DOI: [10.1103/PhysRevE.94.063301](https://doi.org/10.1103/PhysRevE.94.063301)

## I. INTRODUCTION

It is well known that in gas-solid-liquid flows, the fluid interface meets the particle surface and forms a meniscus along the three-phase contact line, of which the local meniscus shape is determined by the contact angle as well as the configuration of different phases. The resulting capillary force may cause the migration, clustering, and adhesion of solid particles. Typical examples include the particle flotation [1] and liquid bridge [2], which are of special interest in various situations of engineering and science. This study will focus on the liquid bridge with fixed volume between spherical particles [3], which can be found in systems at a wide range of spatial scales [4]. The existence of liquid bridges may affect the mechanical property of wet solids and change their behavior, of which the influence is significant for granular particles in dilute [5] and packed [6] states. From an engineering perspective, the modeling of liquid bridges and their capillary actions on surrounding solids is important for recent discrete particle simulations of wet powder processing in, e.g., fluidized beds [7,8], rotating drums [9], and pelletizers [10] to obtain high-fidelity results. Recently, we have developed a macroscopic numerical method for three-phase flows [11], which also requires an accurate modeling of capillary effects between particles and interfaces. For this purpose, a versatile tool for establishing models for liquid bridges under general conditions will be useful.

In the past, a number of studies have been devoted to the analysis and modeling of the liquid bridges between binary

solid surfaces. In some early theoretical studies [12–14], analytical solutions were derived for some special cases, and the necessary conditions to keep bridges stable were discussed. Restrictions come with considerable simplifications by assuming equal particles, symmetric bridge shape about the midplane, and constant radius of the bridge profile. Recently, theoretical efforts have been made to explore the region of existence for concave bridges between two spheres [15], the analytical solution of asymmetric capillary bridge profiles [16], and the equilibrium distance for a force-free bridge between two parallel plates [17]. Very recently, the influence of contact angle hysteresis on formation of stable capillary bridges has also been studied [18,19] in semianalytical approaches.

For their broad relevance in practice, analytical equations of static liquid bridge forces have been suggested neglecting the effects of inertia, viscosity, and gravity. They are generally written as the function of liquid volume, separation distance, and contact angle. A simple equation can be found in the book of Israelachvili [2]. Another equation is proposed by Rabinovich *et al.* [3,20] for symmetric liquid bridges, which is examined experimentally by [21,22]. Those equations have simple forms and they can be efficiently incorporated for wet granular simulations (see, e.g., [10,23]). However, a common problem resides in their applicable range that is restricted to relatively small liquid volumes and contact angles. For example, according to Willett *et al.* [24], their force expression is valid only for volume ratio  $<0.1$  and contact angle  $<50^\circ$ . A more evolved analytical model is derived by Huppmann and Riegger [25]. Their model links the parameters of the liquid bridge profile via the conditions of contact angle, total liquid volume, and circular approximation of the bridge profile by Heady and Cahn [26], and combines them implicitly to form

\*song@dem.t.u-tokyo.ac.jp

†mikio\_sakai@n.t.u-tokyo.ac.jp

a set of nonlinear equations. Once solved, the bridge shape is obtained and consequently the force can be calculated. Similar models have also been developed for asymmetric liquid bridges with unequal particle radii and different contact angles in recent years [27,28]. Improved accuracy can be expected for those models, but the complication and increased cost due to nonlinear solving make them less attractive in practice.

When it comes to the modeling of more general liquid bridges, numerical analysis is an indispensable tool. For static liquid bridges, it is natural to represent the surface by discretization of triangle elements, and perform a nonlinear optimization procedure to minimize the interfacial energy under the constraint of volume conservation [29]. In this respect, the public domain software SURFACE EVOLVER [30] has been used extensively for its ability to heuristically find a surface with minimal energy. A number of past studies have been done by using and adapting the SURFACE EVOLVER: capillary forces and torques between cylinders [31], capillary attraction by asymmetric bridges [32,33], capillary torque by a liquid droplet between two plates [34], evolution of liquid bridges in slit-pore geometry [35], and capillary assembly of nonspherical particles at interfaces [36], to cite a few. The drawback of the SURFACE EVOLVER approach is the limitation to energetic description and static solutions for steady problems. Besides that, the setup of surface mesh is problem specific and the solver needs some user parameters and managements.

In typical gas-solid-liquid flows, the dynamic interactions between different phases are considerably complex. In order to correctly predict the three-phase system behavior, it is necessary to calculate deformation of the interface, fluid motion, and particle movement under capillary actions. Direct numerical simulation (DNS) has become a suitable approach to resolve the complex coupling in those systems including the liquid bridge problem. Unlike static solutions given by the SURFACE EVOLVER, a DNS method solves the governing equations of the motions of fluids, particles, and interfaces. Thus not only the static state but also the dynamic evolution of the system can be obtained to build more comprehensive models of the interaction forces. In recent reports in the literature, some DNS techniques have been developed for gas-solid-liquid systems by using the lattice Boltzmann method (LBM) [37,38], the finite element method (FEM) [39,40], the diffuse interface method (DIM) [41–43], the level set (LS) method [44], and the constrained interpolation profile (CIP) method [45]. They filled the void for many three-phase flow systems, among which the work of Villanueva *et al.* [41] is notable for simulating planar and axisymmetric liquid bridges. However, more work needs to be done to specifically treat the subject of calculating the liquid bridge force on surrounding solid particles in three-dimensional systems. Therefore, the capability and advantage of DNS approaches have not been thoroughly investigated for general liquid bridge problems.

In this study, we present a computational method to perform three-dimensional simulations for gas-solid-liquid flows involving capillary effects. In this method, the THINC/WLIC (tangent of hyperbola for interface capturing with weighed line interface calculation) volume-of-fluid (VOF) method [46] is employed to calculate the shape and mo-

tion of the gas-liquid interface. The solid particles are coupled to the continuous phase by using the immersed boundary (IB) method [47,48] on Cartesian grids. Contact angles are specified as input parameters and implicitly prescribed at three-phase contact lines by using an interface extension technique [49]. The overall algorithm is simple and efficient. It is capable of treating both static and dynamic gas-solid-liquid interactions including the hydrodynamic and capillary forces. This method is referred to as the VOF-IB-DNS method hereinafter.

The objective of this paper is the description of the VOF-IB-DNS method and its application to the numerical analysis of liquid bridges among spherical particles. We present numerical results of the following problems concerning the modeling of liquid bridge problems. First we examine existing liquid bridge force correlations [3,25] with sufficiently small volumes. Next we consider liquid bridges with higher liquid saturation so that some analytical equations may fail to predict the force. The DNS will be compared with experimental data or the SURFACE EVOLVER to justify the results. Besides that, the dependence of the liquid bridge shape and force on the volume, distance, and contact angle is explored. In the third part, the complex liquid bridges connecting multiple particles are simulated, which may be encountered in wet particle layers to form small clusters [50]. This type of liquid bridge, especially the action force, has not been thoroughly studied in the past. Preliminary results of bridge shape and force in triangular and tetrahedral particle structures are presented here. The fourth problem simulates the rupture of a liquid bridge under axial stretching. The rupture distances involving the effects of viscosity and gravity are obtained and compared with reference data. The last test demonstrates the capability of treating dynamic systems where the particle can freely move under the liquid bridge force. It is shown that the dynamic liquid bridge action may become cohesive or repulsive, which is also significantly influenced by the particle motion. We compare the results with past study [41] for different equilibrium states as the contact angle is varied. Therefore, our DNS approach can provide useful information to develop more comprehensive understanding for complex liquid bridge phenomena in wet granular materials, from which the interaction model can be derived without assumptions and restrictions. It may also become a powerful tool for simulating other gas-solid-liquid systems involving particle-interface interactions.

## II. GOVERNING EQUATIONS

We consider a three-phase flow system composed of incompressible Newtonian gas and liquid and the solids particles. For the fluid phases, the Navier-Stokes equation and the continuity equation are written as

$$\rho \left[ \frac{\partial \mathbf{u}}{\partial t} + \nabla \cdot (\mathbf{u}\mathbf{u}) \right] = -\nabla p + \nabla \cdot [\mu(\nabla \mathbf{u} + \nabla \mathbf{u}^T)] + \rho \mathbf{g} + \mathbf{f}_s + \mathbf{f}_p, \quad (1)$$

$$\nabla \cdot \mathbf{u} = 0, \quad (2)$$

where  $\rho$  is density,  $\mathbf{u}$  is velocity,  $p$  is pressure,  $\mu$  is viscosity, and  $\mathbf{g}$  is gravity. The two terms  $\mathbf{f}_s$  and  $\mathbf{f}_p$  indicate the surface tension and fluid-particle interaction, respectively. The surface

tension is given by

$$\mathbf{f}_s = -\sigma\kappa\delta\mathbf{n}, \quad (3)$$

in which  $\sigma$  is the coefficient of surface tension,  $\kappa$  is the curvature,  $\delta$  is a delta function being nonzero at the interface, and  $\mathbf{n}$  is the unit normal vector to the interface.

There are  $N_P$  spherical particles submerged in the fluid, for which the motions are governed by Newton's law of motion:

$$\begin{aligned} m_P \frac{d\mathbf{v}}{dt} &= \mathbf{F}_P + \mathbf{F}_C + m_P \mathbf{g}, \\ I_P \frac{d\boldsymbol{\omega}}{dt} &= \mathbf{T}_P + \mathbf{T}_C, \end{aligned} \quad (4)$$

where  $\mathbf{v}$  is the particle velocity and  $\boldsymbol{\omega}$  is the angular velocity. For a spherical particle  $P$  of radius  $R$ , its volume is  $V_P = (4/3)\pi R^3$ , mass is  $m_P = \rho_P V_P$  with the particle density  $\rho_P$ , and  $I_P = (2/5)m_P R^2$  is the moment of inertia. On the right-hand side,  $\mathbf{F}_C$  and  $\mathbf{T}_C$  are the contact force and torque between solids. The terms  $\mathbf{F}_P$  and  $\mathbf{T}_P$  are the interaction force and torque from surrounding fluids. In the current context of gas-solid-liquid flows, the fluid-particle interactions are made by the surface integral of the pressure and viscous forces over the particle surface  $S$ , and the line integral of capillary force along the contact line CL:

$$\begin{aligned} \mathbf{F}_P &= \int_S (-p\mathbf{I} + \boldsymbol{\tau}) \cdot \mathbf{n}_P dS + \int_{CL} \mathbf{n}_C dL, \\ \mathbf{T}_P &= \int_S \mathbf{r} \times (-p\mathbf{I} + \boldsymbol{\tau}) \cdot \mathbf{n}_P dS + \int_{CL} \mathbf{r} \times \mathbf{n}_C dL. \end{aligned} \quad (5)$$

Herein,  $\boldsymbol{\tau}$  is the viscous stress,  $\mathbf{n}_P$  is the unit normal vector of the particle surface,  $\mathbf{n}_C$  is the unit vector of the capillary action, and  $\mathbf{r} = \mathbf{x} - \mathbf{x}_P$  is the relative position from point  $\mathbf{x}$  to the particle center  $\mathbf{x}_P$ .

Those momentum equations are supplemented by the compatible nonslip boundary condition,

$$\mathbf{u} = \mathbf{u}_P = \mathbf{v} + \boldsymbol{\omega} \times (\mathbf{x} - \mathbf{x}_P), \quad (6)$$

at point  $\mathbf{x}$  on the particle surface or inside the particle, where  $\mathbf{u}_P$  is the solid velocity. For the meniscus attached to the solid surface, a static contact angle boundary condition is prescribed as

$$\mathbf{n} \cdot \mathbf{n}_P = \cos \theta, \quad (7)$$

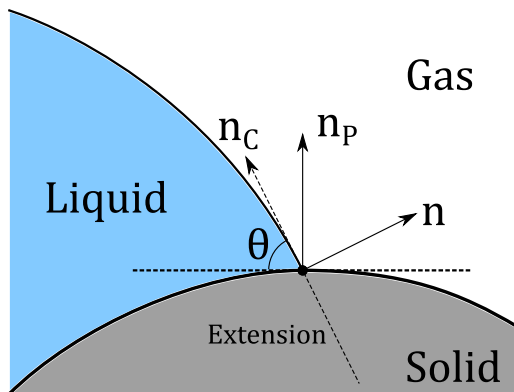


FIG. 1. Contact angle boundary condition at gas-solid-liquid three-phase point.

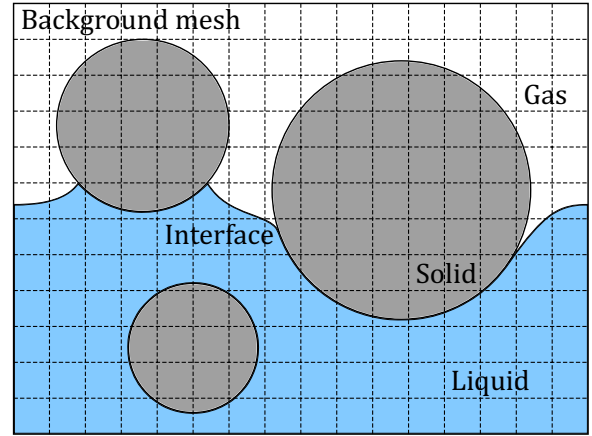


FIG. 2. DNS grid for gas-solid-liquid flows. Calculation is based on a Cartesian mesh, for which the grid size must be finer than the characteristic length of the particle or meniscus.

in which  $\theta$  is the contact angle. See Fig. 1 for a two-dimensional schematic diagram of their definitions.

### III. NUMERICAL METHODOLOGY

Now we briefly describe the DNS method developed in this study. It solves the governing equations summarized in the preceding section for gas-solid-liquid flows without employing any specific models for their interactions. The modeling of the fluid-particle system adopts the IB method [47,48], in which a uniform Cartesian mesh covers the entire domain for both fluid and particle phases. A schematic diagram of this computational setup is illustrated in Fig. 2. The grids need not conform to curved fluid interfaces or solid surfaces. The grid size is required to be fine enough to resolve the important characteristics of the underlying flow.

#### A. Multiphase flow solver

The immiscible interface separating the gas and liquid phases is indicated by the so-called VOF function  $\varphi$ . By definition, we have  $\varphi = 0$  in the gas,  $\varphi = 1$  in the liquid, and  $0 < \varphi < 1$  near the interface. Using the VOF function, the fluid density and viscosity are calculated by

$$\begin{aligned} \rho &= \varphi \rho_l + (1 - \varphi) \rho_g, \\ \mu &= \varphi \mu_l + (1 - \varphi) \mu_g, \end{aligned} \quad (8)$$

with the subscripts  $l$  and  $g$  denoting the liquid and gas phases, respectively. The motion of the fluid interface is described by the following advection equation:

$$\frac{\partial \varphi}{\partial t} + \mathbf{u} \cdot \nabla \varphi = 0. \quad (9)$$

It is solved by using the THINC-WLIC VOF method [46] to sharply capture the fluid interface. The VOF functions  $\varphi$  in the interfacial regions are periodically redistributed by using the method described in our previous work [51] to conserve the fluid volume. Similar methods of volume correction have also been used by other authors [43,44,52] to eliminate accumulative conservation error for long-time simulations.

The static contact angle (7) at three-phase contact lines is treated by using the extension approach [49] which can readily apply to solid boundaries with arbitrary shapes. In this approach, the VOF function is extrapolated into the solid domain along a selected direction, so that a continuous interface is formed across the solid surface and the contact angle boundary condition is implicitly satisfied. The numerical procedure consists in solving a special advection equation,

$$\frac{\partial \varphi}{\partial \tau} + \mathbf{u}_e \cdot \nabla \varphi = 0, \quad (10)$$

in solid domains with fictitious time step  $\Delta \tau = \Delta x$  using a semi-Lagrangian upwind scheme [51]. Herein,  $\mathbf{u}_e$  is an extension velocity for interface extrapolation, which is constructed parallel but inverse to the desired capillary force vector by

$$\mathbf{u}_e = \begin{cases} -\frac{\mathbf{n}_p - \cot(\pi - \theta) \mathbf{n}_2}{|\mathbf{n}_p - \cot(\pi - \theta) \mathbf{n}_2|} & \text{if } c < 0 \\ -\frac{\mathbf{n}_p + \cot(\pi - \theta) \mathbf{n}_2}{|\mathbf{n}_p + \cot(\pi - \theta) \mathbf{n}_2|} & \text{if } c > 0 \\ -\mathbf{n}_p & \text{otherwise} \end{cases}, \quad (11)$$

with

$$\mathbf{n}_1 = \frac{\mathbf{n} \times \mathbf{n}_p}{|\mathbf{n} \times \mathbf{n}_p|}, \quad \mathbf{n}_2 = \frac{\mathbf{n}_1 \times \mathbf{n}_p}{|\mathbf{n}_1 \times \mathbf{n}_p|}, \quad \text{and } c = \mathbf{n} \cdot \mathbf{n}_2. \quad (12)$$

For example, in Fig. 1 near the contact point, the extension velocity  $\mathbf{u}_e$  is oriented toward the solid side away from the capillary vector  $\mathbf{n}_c$  determined by the interface vector  $\mathbf{n}$ , the solid vector  $\mathbf{n}_p$ , and the contact angle  $\theta$ . The extension approach has made the contact angle treatment simple, since it does not require locating the position of the contact line explicitly. It can also be implemented for nonspherical particles without much difficulty if the particle shape and surface normal can be calculated efficiently. We note that extending the interface by Eq. (10) will change the contact line position on the solid surface while keeping the contact angle prescribed. This is equivalent to introduce a finite slip distance numerically at the length scale of grid spacing. In this way, the dilemma between the moving contact line and the nonslip velocity condition could be circumvented.

Particularly, we comment on the treatment of dynamic contact angle. In recent years, some authors introduced fundamental hydrodynamic models for dynamic wetting on planar surfaces; see, e.g., Afkhami *et al.* [53] with Cox's asymptotic analysis [54], Yokoi *et al.* [55] with Tanner's law [56], Griebel and Klitz [57] with Shikhmurzaev's interface formation model [58], and the review and comparison by Legendre and Maglio [59]. It is, however, not known how their modeling applies to other problems or general geometries. For this sake, many recent numerical studies on multiphase systems choose to only use static contact angles; see, e.g., [37,60–64]. Similarly in this study, we consider static contact angle conditions for liquid bridge problems without hysteresis effects and postpone the implementation of a numerical model for dynamic contact angle.

The basic fluid solver is similar to that used in our previous study [51]. The governing equations are discretized on a staggered grid where velocity components are defined on cell faces and other scalars are defined at cell centers. The spatial derivatives are calculated by second-order central difference. A fractional-step method is used to advance the Navier-Stokes

equation (1) subject to the incompressible condition (2). At the  $n$ th step of the simulation, the work-flow algorithm is written as follows.

$$\frac{\mathbf{u}^{(1)} - \mathbf{u}^n}{\Delta t} = -\left[ \frac{3}{2} \nabla \cdot (\mathbf{u}\mathbf{u})^n - \frac{1}{2} \nabla \cdot (\mathbf{u}\mathbf{u})^{n-1} \right] + \frac{1}{\rho} \left( \frac{1}{2} \nabla \cdot \mu \nabla \mathbf{u}^{(1)} + \frac{1}{2} \nabla \cdot \mu \nabla \mathbf{u}^n \right), \quad (13)$$

$$\mathbf{u}^{(2)} = \mathbf{u}^{(1)} + \Delta t \mathbf{g} + \frac{\Delta t}{\rho} \mathbf{f}_s, \quad (14)$$

$$\nabla \cdot \left( \frac{1}{\rho} \nabla p \right) = \frac{1}{\Delta t} \nabla \cdot \mathbf{u}^{(2)}, \quad (15)$$

$$\mathbf{u} = \mathbf{u}^{(2)} - \frac{\Delta t}{\rho} \nabla p. \quad (16)$$

In Eq. (13), we use an Adams-Bashforth method for the convective term and a Crank-Nicolson method for the viscous term, respectively. The surface tension  $\mathbf{f}_s$  in Eq. (14) is calculated by the balanced continuous surface force (CSF) model [65] which has been tested in Ref. [51]. The variable-coefficient Poisson equation (15) is solved by using a multigrid preconditioned conjugate gradient (MGPCG) method. Finally Eq. (16) projects the velocity to a discretely divergence-free space. The stable time step of the algorithm is limited by the explicit Courant-Friedrichs-Lewy (CFL) condition and the surface tension computation.

## B. Fluid-particle interaction

The IB method is employed to achieve the coupling between particles and fluids. Because all phases are simulated on the same grid, the volume fraction  $\varphi_p$  is used to identify the existence of solids in each numerical cell. Similar to the VOF function,  $\varphi_p = 0$  in the fluid,  $\varphi_p = 1$  in the solid, and  $0 < \varphi_p < 1$  near the particle surface. Hence its 0.5 contour smoothly represents the particle shape. In the simulation, an intermediate velocity is first obtained by the fluid solver for the whole domain, which does not satisfy the rigid motion (6) for solids in general. This error is explicitly corrected by the IB forcing term  $\mathbf{f}_p$  as

$$\mathbf{f}_p = \rho \frac{\varphi_p (\mathbf{u}_p - \mathbf{u})}{\Delta t}. \quad (17)$$

Subsequently, adding the action of  $\mathbf{f}_p$  to  $\mathbf{u}$  yields an updated velocity at the next time step:

$$\mathbf{u}^{n+1} = \mathbf{u} + \frac{\Delta t}{\rho} \mathbf{f}_p = \varphi_p \mathbf{u}_p + (1 - \varphi_p) \mathbf{u}. \quad (18)$$

With the definition of  $\varphi_p$ , it is easy to find that for fluid domains where  $\varphi_p = 0$  the effect of  $\mathbf{f}_p$  vanishes, whereas in regions with  $\varphi_p > 0$ , the velocity is modified by a linear interpolation of local fluid and solid velocities. Particularly, the velocity will be completely replaced by the solid velocity  $\mathbf{u}_p$  inside solid particles ( $\varphi_p = 1$ ).

For the solid phase, the problem is to evaluate correspondingly the interaction forces for distinct particles. In the present DNS method, their forms are derived by considering the integral of fluid actions over the particle surface to ensure the consistency with coupled fluid equations. For convenience,

we let  $\tau$  denote the deviatoric viscous stress and introduce the tensorial form of the surface tension force via a capillary pressure tensor  $\Pi$  [66] satisfying

$$\begin{aligned}\mathbf{f}_s &= -\nabla \cdot \Pi, \\ \Pi &= -\sigma(\mathbf{I} - \mathbf{n} \otimes \mathbf{n})\delta.\end{aligned}\quad (19)$$

The total fluid force is thus defined by the integral of the multiphase stresses over the particle surface  $S$ ,

$$\mathbf{F}_P = \int_S (-p\mathbf{I} + \tau) \cdot \mathbf{n}_P dS + \int_S (-\Pi) \cdot \mathbf{n}_P dS, \quad (20)$$

in which the terms on the right-hand sides are the hydrodynamic and capillary forces, respectively. In order to eliminate the numerical intricacy of surface integration on nonconforming IB meshes [47], it is equivalently transformed into a volume integral for the particle body via the Gauss divergence theorem provided that all stress terms are continuous across the particle surface,

$$\mathbf{F}_P = \int_P \nabla \cdot (-p\mathbf{I} + \tau) dV + \int_P \nabla \cdot (-\Pi) dV. \quad (21)$$

Although it is now possible to calculate the interaction force  $\mathbf{f}_P$  by performing numerical quadrature for each term in the equation above, we suggest an alternative approach which is more efficient. We start with the momentum equation (1) rewritten as

$$\rho \frac{D\mathbf{u}}{Dt} = -\nabla p + \nabla \cdot \tau + \rho \mathbf{g} - \nabla \cdot \Pi + \mathbf{f}_P. \quad (22)$$

Integrating on both sides over the solid domain and rearranging the equation to isolate stress terms, we arrive at an alternative relationship useful for  $\mathbf{F}_P$ :

$$\mathbf{F}_P = - \int_P \mathbf{f}_P dV - \int_P \rho \mathbf{g} dV + \int_P \rho \frac{D\mathbf{u}}{Dt} dV. \quad (23)$$

The first term is the integration of the IB forcing  $\mathbf{f}_P$  inside the particle domain, before which the minus sign indicates the reciprocal relation of being an action and reaction pair between fluid and particle phases. Therefore, it is identified as the total fluid-particle interaction including both hydrodynamic and capillary forces. The second term is apparently the hydrostatic buoyancy separated from the dynamic actions. The last term is due to the acceleration of the particle motion, which is dropped for particles with prescribed motions or negligible inertial effects. In a similar fashion, we are able to derive the torque of fluid forces on a single particle as

$$\mathbf{T}_P = - \int_P (\mathbf{x} - \mathbf{x}_P) \times \mathbf{f}_P dV. \quad (24)$$

In each time step, we first solve the extended Navier-Stokes equation and calculate the IB forcing term  $\mathbf{f}_P$  on the fluid meshes. In the next stage, integrals contained in the interaction force (23) and torque (24) are computed for individual solid particles by using the solid volume fraction  $\varphi_P$  as weights:

$$\begin{aligned}\mathbf{F}_P &= - \sum \varphi_P (\mathbf{f}_P + \rho \mathbf{g}) \Delta V, \\ \mathbf{T}_P &= - \sum \varphi_P (\mathbf{x} - \mathbf{x}_P) \times \mathbf{f}_P \Delta V,\end{aligned}\quad (25)$$

in which the summations are taken over the numerical cells accommodated by the bounding box of the particle and  $\Delta V$  is

the cell volume. We remark that the present method extends our previous study [51] to direct calculation of interactions between multiphase flow and solid particles in light of Eqs. (17), (23), and (24). Consequently, it allows for solving degrees of freedom associated with particle motion, whereas only prescribed boundary movements are handled by [51]. In addition, this treatment of multiphase fluid-particle interaction can be applied to nonspherical solids without modification, as long as their shapes are discretized in a volume-of-solid way on the fluid grid.

### C. Particle dynamics

The present method contains a contact force model for particle-particle and particle-wall interactions. The contact force  $\mathbf{F}_C$  and torque  $\mathbf{T}_C$  are based on the discrete element method (DEM) [67] widely applied in granular material simulations. In the DEM, an artificial overlap sufficiently smaller than particle radius is allowed for two solids in contact, for which the interaction is computed by a Voigt model consisting of spring, dashpot, and friction slider. The details and applications can be found in our previous studies [11,68,69]. Compared with other “*ad hoc*” models implemented for particle suspensions (e.g., [70–72]), the DEM is advantageous to treat viscoelastic collisions and dissipative frictions between solid particles. Recently, it has been also justified to use the DEM for modeling particle roughness in dense suspensions [73–75]. In this study, the contact force mainly serves to prevent nonphysical penetration of particles connected by cohesive liquid bridges. Therefore, the DEM parameters are not discussed in detail.

Once the total force and torque are obtained for a particle, the Newton equations (4) can be integrated to update the particle states. If the particle is fixed or subject to prescribed motion, we simply skip this part. The symplectic Euler scheme is used:

$$\begin{aligned}\mathbf{v}_P^{n+1} &= \mathbf{v}_P^n + \Delta t (m_P \mathbf{g} + \mathbf{F}_C^n + \mathbf{F}_P^n) / m_P \\ \mathbf{x}_P^{n+1} &= \mathbf{x}_P^n + \Delta t \mathbf{v}_P^{n+1} \\ \omega_P^{n+1} &= \omega_P^n + \Delta t (\mathbf{T}_C^n + \mathbf{T}_P^n) / I_P\end{aligned}\quad (26)$$

The symplectic Euler scheme yields satisfactory results for the present study. It can be easily replaced by another integrator (e.g., the second-order Adams-Bashforth scheme) targeting higher-order accuracy. Additionally, we note that the algorithm can be extended to nonspherical particles in a straightforward way, which will be taken as a future development.

### D. Related work

In the past, some numerical techniques have been developed to resolve three-phase flows involving capillary actions. The lattice Boltzmann method (LBM) has been first used to study the lateral capillary force between two-dimensional objects such as squares [76] and circles [37,77], and simulate three-dimensional problems including the self-assemblies of colloidal particles on substrate [78] and spreading drops containing particle suspensions [71]. Recently, the LBM is applied to spheroidal particles captured at fluid-fluid interfaces for evaluating the detachment energy [79] and simulating their

alignment under magnetic fields [80,81]. In the LBM, circular particles are directly mapped onto lattice points, resulting in a stair-shaped representation of the particle surface at the discrete space. The multiphase LBM may also suffer from some numerical stability problems for gas-liquid flows with high-density ratios. Some authors coupled the LBM with VOF-based interface tracking [82] or phase-field formulation [38,83] to simulate flows involving high-density ratios or free surfaces.

The finite element method (FEM) has also been used to simulate spheres and disks floating on free surfaces [39,84] and liquid bridges between two circular disks experiencing coaxial stretching [40]. In the FEM, the numerical algorithm is considerably complicated. Moreover, FEM using body-fitted grids needs frequent mesh manipulation and regeneration for moving particle simulations, which is difficult to implement and computationally expensive in three-dimensional cases.

The diffuse interface method (DIM) with phase-field formulations has particular strength in modeling complex fluids involving multiple components and phase separations. Villanueva *et al.* simulated the multiphase flow system during liquid sintering [41]. Their special contribution is the computation of particles connected by liquid bridges in two-dimensional and axisymmetric systems. However, the equilibrium state of the liquid bridge between particle pairs did not agree well with theoretical predictions. Their approach cannot calculate the liquid bridge force for a single particle, either. By using the so-called diffuse interface field approach (DIFA) [42], Cheng and Wang [43] simulated the formation of two-dimensional capillary bridges between packed particles during phase separation of liquids. However, their interface solver is not coupled with a dynamic solver for fluid and particle motions. As a result, the liquid bridge force firming the particle structure cannot be obtained.

Very recently, several computational fluid dynamics (CFD) approaches have been developed to allow for efficient DNS of three-phase flows on fixed grids. Fujita *et al.* [44,85] described their immersed free surface model based on the level set (LS) method and simulated the capillary interactions among drying particle suspensions. We find that our method shares some common aspects with theirs, especially for the treatment of the contact angle and the capillary force. Kan *et al.* [45] treated capillary interactions based on the constrained interpolation profile (CIP) modeling of three-phase problems [86,87]. They studied the particle adhesion by liquid bond after a head-on collision. Unlike their method requiring evaluation of distinct fluid actions, in the present approach both hydrodynamic and capillary forces are taken into account by a single IB forcing term. Another different point is that our interface modeling is based on the VOF method, which may conserve the liquid volume to a better accuracy than the LS or CIP method.

#### IV. PROBLEM DESCRIPTION

As specified, we study liquid bridges between spherical particles. Figure 3 depicts two fundamental situations of liquid bridges with different wettability of spherical surfaces separated by distance  $H$ . The left part shows a hydrophobic case where the contact angle  $\theta > \pi/2$  and the sectional shape of the liquid bridge is convex; the right part shows a hydrophilic

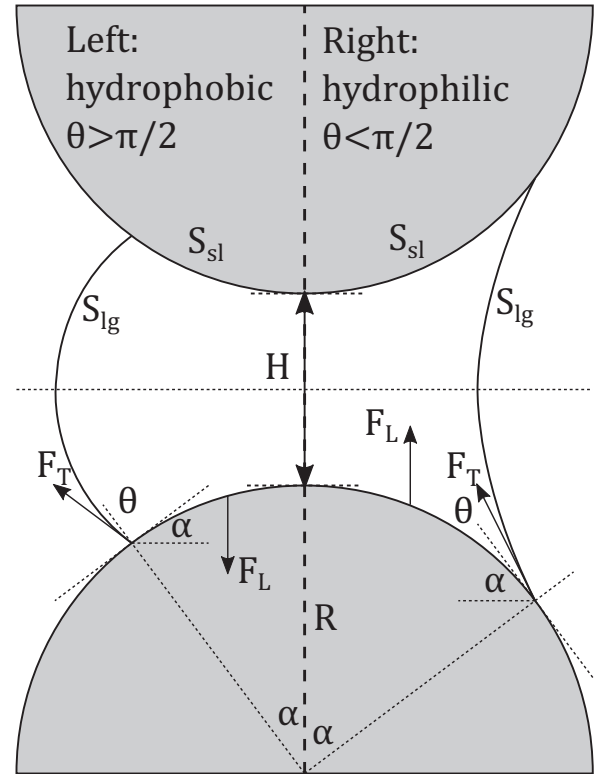


FIG. 3. Liquid bridges between two spheres: typical hydrophobic case (left) and hydrophilic case (right).

bridge with  $\theta < \pi/2$  and a concave surface. We note that Fig. 3 is at most a demonstration of typical bridge shapes depending on contact angles. It is apparent that a hydrophilic surface does not necessarily give rise to concave bridges.

#### A. Liquid bridge force

We consider the force on the spheres exerted by the liquid bridge. The static liquid bridge force should be a function of the bridge volume  $V_{LB}$ , the particle separation distance  $H$ , and the contact angle  $\theta$ . It can be defined by two methods, i.e., the geometric approach and the energetic approach [22]. The former models the liquid bridge action  $\mathbf{F}_{LB}$  by directly decomposing it into contributions of the Laplace pressure  $\mathbf{F}_L$  and the surface tension  $\mathbf{F}_T$ :

$$\mathbf{F}_{LB} = \mathbf{F}_L + \mathbf{F}_T. \quad (27)$$

The Laplace term  $F_L$  is the surface force by integrating the liquid pressure and ambient gas pressure over the sphere, while the tension term  $F_T$  is a singular force found along the contact line. As illustrated in Fig. 3, the direction of  $F_L$  may vary depending on the shape of the bridge: For convex bridges the Laplace pressure is positive and  $F_L$  is repulsive, while for concave bridges the pressure is negative and the corresponding  $F_L$  is attractive. On the other hand, the tensile force  $F_T$  always tends to pull spheres together. In principle, both terms can be determined geometrically provided that the profile of the bridge shape is known. Moreover, in an

axisymmetric liquid bridge, the forces are reduced to scalars by their axial components:  $F_{LB}$ ,  $F_L$ , and  $F_T$ . In this study, it is designated that  $F > 0$  for attractive forces and  $F < 0$  for repulsive forces.

The energetic definition of liquid bridge force considers the following interfacial free energy  $W$ :

$$W = \sigma(S_{gl} - S_{sl} \cos \theta). \quad (28)$$

Here  $S_{gl}$  and  $S_{sl}$  are the gas-liquid and solid-liquid contact areas, respectively (see Fig. 3). The minimal surface energy is associated with the static configuration of the liquid bridge. According to the virtual work principle, the variation of  $W$  with respect to some perturbed displacement  $\Delta h$  of particles gives the total liquid bridge force, i.e.,

$$F_{LB} = -\frac{\Delta W}{\Delta h}. \quad (29)$$

The value of  $F_{LB}$  can be readily calculated by numerical difference. For the axisymmetric bridge between a pair of particles, the virtual displacement  $\Delta h$  coincides with the incremental separation distance  $\Delta H$ , but this might not be the case for the liquid bridge among multiple particles.

If the particles are allowed to move, the liquid bridge force may also depend on dynamic parameters such as fluid density, viscosity, and particle velocity. In that case, the total action of the liquid bridge should be given by the integral of fluid stress and surface tension over the particle as in Eq. (20). Besides the capillary interaction, the relative motion of particles causes the liquid bridge to be squeezed or stretched, which will introduce a damping effect owing to lubrication mediated by the bridge [88,89].

### B. Characteristic quantities

We present dimensionless results for the liquid bridge problem if not specified. The spatial dimensions are divided by the characteristic length  $L_0 = R$ , area  $S_0 = R^2$ , and volume  $V_0 = R^3$ , respectively. The dimensionless force and pressure are obtained with the factors  $F_0 = \sigma R$  and  $P_0 = \sigma/R$ . The scale of the interfacial energy is given by  $W_0 = \sigma R^2$ . Specifically, the volume of the liquid bridge is described as the ratio with respect to the sphere volume for convenience.

The DNS involves the initialization, relaxation, and convergence of the liquid bridge toward a balanced state, which is essentially a dynamic process. Provided a characteristic velocity  $U$ , important dimensionless numbers are the capillary number  $Ca = \mu U/\sigma$  (relative effect of viscosity vs surface tension), the Weber number  $We = \rho U^2 R/\sigma$  (inertia vs surface tension), and the Bond number  $Bo = \rho g R^2/\sigma$  (gravity vs surface tension, if the gravity is present). The well-known Reynolds number is given by  $Re = We/Ca$  (inertia vs viscosity).

Among the characteristic quantities, a natural choice of characteristic velocity  $U$  is the speed of a solid particle. If a particle is fixed or the velocity is not known *a priori*, it can be defined on the capillary scale  $U = \sigma/\mu$ . The density ratio and viscosity ratio between liquid and gas may affect the dynamic behaviors without changing the equilibrium state of the liquid bridge. In this study, the density and viscosity ratios are typically chosen as high as 100:1 to show the capability for modeling real gas-liquid flows in wet granular systems. This

results in flow behaviors dominated by the liquid phase, but it should have no appreciable influence on the static shape and force of the liquid bridge. On the other hand, those parameters between two comparable fluid phases may be important in liquid-liquid systems. Some results of those low-density ratio flows may be found in past studies using the lattice Boltzmann method or the phase-field method; see, e.g., [37,41,71].

### C. Simulation and force calculation

The computational domain is a box accommodating the particles and liquid bridge while the rest of the void is filled with gas. On the domain borders transparent or symmetric boundary conditions are set. The liquid bridge is initialized by a simple shape (e.g., cylinder for dual particles and sphere for multiple particles) with prescribed volume, and then it is released for free motion. If static problems are concerned, we freeze the particles and allow the bridge to relax until an equilibrium state is reached. The numerical Reynolds number is chosen to be relatively small at an order of  $Re \sim 10^1$  to accelerate the convergence.

In our DNS method, the overall interaction force can be collected straightforwardly for individual particles during the simulation, i.e., the fluid-particle force of Eq. (23). Specifically for static problems, this is equivalent to the calculation of total liquid bridge force with the geometric approach (27). On the other hand, the energetic approach is also available by taking the differentiation for the interfacial energy (28) in a postprocessing stage. Two approaches have been tested and similar results are obtained, which proves their equivalence as argued by [22]. In addition, reference solutions are generated by using the SURFACE EVOLVER, from which the interfacial shape and energy can be found but the action force is, however, not directly available. In that case, we use the geometric definition to calculate the force for simple axisymmetric particle pairs and the energetic definition for multiple particles. It is emphasized that the present DNS method can be applied to dynamic problems while the SURFACE EVOLVER approach is restricted to static configurations.

## V. MODEL TEST

### A. Basic spreading behavior

The dynamic simulation of gas-solid-liquid problems requires calculating the fluid motions over a solid surface. We present an example for the basic spreading behavior of a droplet on a fixed spherical particle. This problem is studied experimentally and numerically using commercial CFD software by Mitra *et al.* in [90]. The problem setup is composed of a spherical droplet whose diameter is  $a = 2.1$  mm and a solid particle whose diameter is 10 mm. They are kept just in touch with each other; see the inset of Fig. 4. The liquid is isopropyl alcohol with density  $\rho_l = 780.8$  kg/m<sup>3</sup> and viscosity  $\mu_l = 0.0022$  Pa s. The air phase has density  $\rho_g = 1.184$  kg/m<sup>3</sup> and viscosity  $\mu_g = 1.82 \times 10^{-5}$  Pa s. The surface tension coefficient is  $\sigma = 0.0236$  N/m, and the contact angle is set to  $\theta = 0.5^\circ$ . The effect of contact angle hysteresis can be neglected as the contact angle is small. The droplet hits the particle with initial velocity  $U = 0.45$  m/s. This gives a

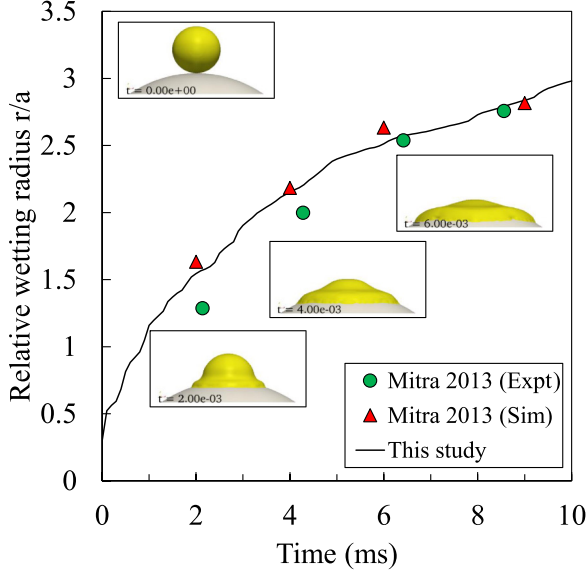


FIG. 4. Spreading of a droplet on spherical particle surface. Reference data are obtained from Mitra *et al.* [90].

Weber number of  $We = 14.1$ , which is sufficiently close to the condition in the literature [90] ( $We \sim 15$ ).

The spreading behavior of the droplet is computed by using the present DNS method with grid size  $\Delta x = 1/16$  mm and time step  $\Delta t = 5.0 \times 10^{-6}$  s. We compared the spreading radius  $r$  (normalized by the initial diameter  $a$ ) on the solid surface with the values obtained from [90]. The results are plotted as a function of time in Fig. 4, together with several snapshots (at time instant  $t = 0, 2, 4, 6$  ms) inserted as insets. The relative spreading radius  $r/a$  starts with zero (initial state) and quickly expands over a factor of 2 on the hydrophilic surface. Its evolution well agrees with the experimental and numerical data of [90]. It is thus shown that the present DNS method can give reasonable prediction for gas-liquid flow moving on a solid surface, such as the nonequilibrium liquid bridge between particles.

**B. Convergence of force calculation**

We focus on the liquid bridge problem from now on. Prior to detailed validation and investigation in the next section, here we carry out a grid convergence study for the force calculation. A static liquid bridge between two equal particles is chosen as a test problem, for which the relative liquid volume is  $V_{LB}/V_P = 0.2$ , the particle separation distance is  $H/R = 0.2$ , and the contact angle is  $\theta = 36^\circ$ . For the current condition, a reference value of the dimensionless liquid bridge force is  $F_{Ref} = 2.67$  (attractive) when computed by the SURFACE EVOLVER.

This problem is calculated to check the force results by using meshes gradually refined. For convenience, the grid spacing is given in terms of the particle diameter  $D$  by  $D/\Delta x = 10, 20, 40, 60$ , and  $80$ , respectively. The results are summarized and compared with the reference value in Table I. The convergence of force calculation can be clearly confirmed. Figure 5 indicates that the convergence rate is close to first order. Particularly, on the coarsest mesh ( $D/\Delta x = 10$ ) the relative error is up to 20%; on a medium grid of  $D/\Delta x = 40$  the error is below 7%, showing qualitative agreement with

TABLE I. Convergence of liquid bridge force calculation toward reference solution.

$D/\Delta x$	$H/\Delta x$	DNS	Evolver	Error
10	2	2.15	2.67	19.5%
20	4	2.35		12.2%
40	8	2.49		6.84%
60	12	2.55		4.51%
80	16	2.58		3.55%

the reference solution. Therefore, based on a compromise between efficiency and accuracy, we have typically 30–40 computational cells along the diameter of a single particle when choosing the spatial resolution in the following studies.

**VI. RESULTS AND DISCUSSION**

**A. Small-volume liquid bridge**

The first part is an examination of the existing liquid bridge force correlations. We consider the two analytical models for the liquid bridge between two equal spheres by Rabinovich *et al.* [3]. In model A the liquid bridge force is given by

$$F_{LB}^A = \frac{2\pi R\sigma \cos \theta}{1 + H/2d}, \tag{30}$$

where

$$d = (H/2)[-1 + \sqrt{1 + 2V_{LB}/(\pi RH^2)}] \tag{31}$$

is the immersion height between the sphere tip and the contact ring. Model B adds a correction to the previous one by

$$F_{LB}^B = F_{LB}^A + 2\pi R\sigma \sin \alpha \sin(\alpha + \theta), \tag{32}$$

where the embracing angle  $\alpha$  subtending the contact ring position and axial direction is demonstrated in Fig. 3. Rabinovich claims that the extra term on the right-hand side of model B

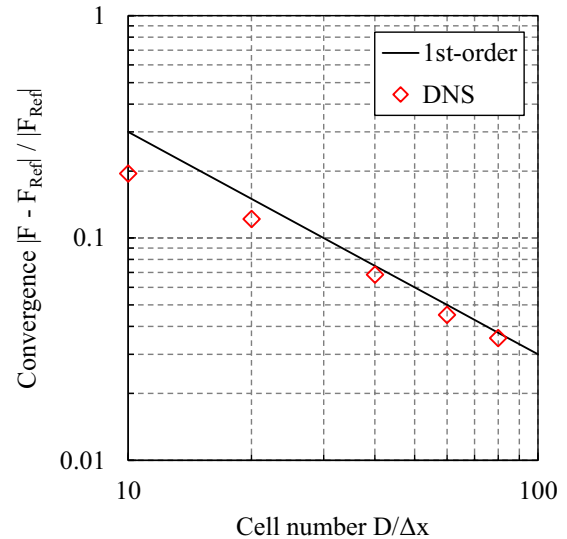


FIG. 5. Convergence of liquid bridge force calculation toward reference solution. The line of first-order rate is drawn as a guide to the eye.

takes the tensile term into account for the total liquid bridge force, which has been invalidated experimentally by [22] and will be tested by the present DNS. The previous equations are mainly developed for liquid bridges with rather small volumes or contact angles. In [3], the derived equations are compared with experimental data with liquid volume <0.05% of the particle volume and contact angle <10°. The validation study [22] shows results of a relative volume of 4.2% and a contact angle of 15°. Another semianalytical model, proposed by Willett *et al.* [24], is valid for a liquid bridge up to 2.4% of the particle volume and a 50° contact angle. Therefore, the typical range of the analytical model is designated as a liquid amount below approximately 5% of a single particle’s volume in the current work.

Besides the two simple models, we also compare a more complicated model C derived by Huppmann and Riegger [25] based on the circular approximation of the bridge profile [26]. In this model, the liquid bridge force is given by the summation of the pressure term and the tension term as

$$F_{LB}^C = \pi R^2 \sin^2 \alpha \Delta p + 2\pi R \sigma \sin \alpha \sin(\alpha + \theta). \quad (33)$$

The pressure jump  $\Delta p$  is given by the Laplace formula:

$$\Delta p = \sigma (\rho_2^{-1} - \rho_1^{-1}), \quad (34)$$

and the two principle curvature radii  $\rho_1$  and  $\rho_2$  in axial and meridional planes are calculated, respectively, as

$$\begin{aligned} \rho_1 &= R \sin \alpha - [R(1 - \cos \alpha) + H/2] \frac{1 - \sin(\alpha + \theta)}{\cos(\alpha + \theta)} \\ \rho_2 &= \frac{R(1 - \cos \alpha) + H/2}{\cos(\alpha + \theta)}. \end{aligned} \quad (35)$$

The equations are closed by the conservation of total liquid volume:

$$\begin{aligned} V_{LB} &= 2\pi [\cos(\alpha + \theta) - (\pi/2 - \alpha - \theta)] (\rho_2^3 + \rho_1 \rho_2^2) \\ &+ \pi \rho_1^2 \rho_2 \cos(\alpha + \theta). \end{aligned} \quad (36)$$

Therefore, Eqs. (35) and (36) are coupled in a nonlinear way, and they must be solved for the key parameter, viz. the embracing angle  $\alpha$ , to obtain  $\rho_1$  and  $\rho_2$  inserted into the force equation (33). This implicit nature limited its practical usage in discrete particle simulations.

We begin by investigating the symmetric liquid bridge with 0.5% volume out of a single sphere. The separation distance between spheres is changed by  $H/R = 0.05, 0.1, 0.15$ , and  $0.2$  to obtain the liquid bridge force correspondingly. The influence of the contact angle is tested by setting its value to  $\theta = 15^\circ, 30^\circ$ , and  $60^\circ$  respectively. For this problem, the grid spacing is determined to resolve the small meniscus of the bridge, so we use a small cell size  $R/\Delta x = 90$ . Because of the restriction of computational cost, the problem symmetry is used to reduce the size of the computational domain, and the liquid-gas density ratio is set to unity to accelerate the solution of the pressure equation.

Figure 6 plots the forces obtained with different separation distances and contact angles. In general, the liquid bridge force decreases monotonically with increasing distance, which is recovered by all approaches. DNS and the SURFACE EVOLVER results agree well, and the analytical model A is also able to calculate the force consistently. The agreement between model A and numerical results is most remarkable at small separation distances and contact angles. As the distance or contact angle increases, the analytical model slightly deviates from

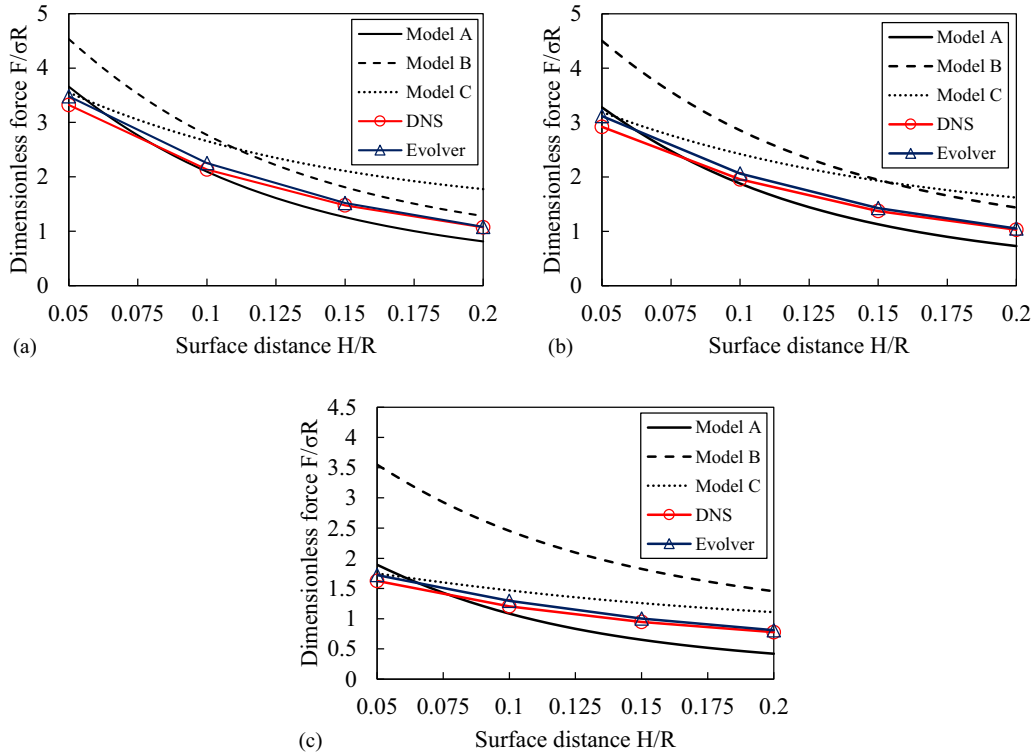


FIG. 6. Forces of a small-volume liquid bridge with different contact angles: (a)  $\theta = 15^\circ$ , (b)  $\theta = 30^\circ$ , (c)  $\theta = 60^\circ$ .

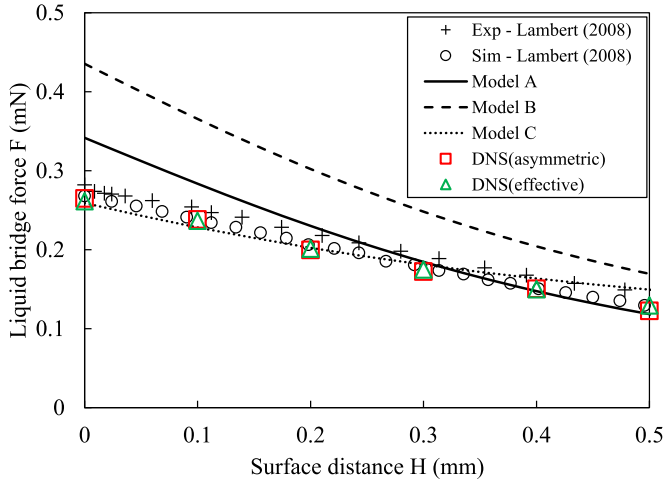


FIG. 7. Comparison of forces by an asymmetric liquid bridge. The reference plots of experiment and simulation are measured from Lambert *et al.* [22].

numerical results. On the other hand, model B yields stronger attraction due to the extra term which is always positive. This systematic error becomes even larger with increasing contact angle, for which the pulling effect stemming from the extra term becomes significant. As for the more complicated model C, it is close to the numerical calculation when the separation is small in general, but it does not seem to work very well if the distance is large. This implies that the circular approximation of the liquid bridge profile may not be accurate for the current small volumes.

In another test, we computed the asymmetric liquid bridge problem of Lambert *et al.* [22], in which they experimentally measured the millimeter-scale adhesion between two spheres with different physical properties. For validation against their data, our results are also presented in dimensional forms. For the problem setup, the lower sphere has radius  $R_1 = 2$  mm and contact angle  $\theta_1 = 0^\circ$  (set to  $0.5^\circ$  in DNS), and the upper sphere has radius  $R_2 = 3.95$  mm and contact angle  $\theta_2 = 14.3^\circ$  (set to  $15^\circ$  in DNS). The volume of the liquid bridge is  $V_{LB} = 1.4$  mm<sup>3</sup>, which is 4.2% of the lower sphere volume in percentage. The surface tension is 0.0208 N/m. Since the asymmetric bridge involves unequal radii and contact angles of solid surfaces, an effective configuration [2] is introduced for adapting the analytical models: The effective radius is  $R_{\text{eff}} = 2R_1R_2/(R_1 + R_2)$  and the effective contact angle satisfies  $\cos\theta_{\text{eff}} = (\cos\theta_1 + \cos\theta_2)/2$ , giving  $R_{\text{eff}} = 2.66$  mm and  $\theta_{\text{eff}} = 10.1^\circ$ . Both the asymmetric case and the effective case are calculated by using the DNS method.

The force-distance relationships obtained by using different approaches are plotted in Fig. 7, where the plus symbols are the experimental data in Lambert *et al.* [22], and the circles are their simulation results using the SURFACE EVOLVER [91]. For separation distances varying from zero to 0.5 mm (or  $0.25R_1$ ), our DNS results of both asymmetric and effective cases agree well with the data of Lambert *et al.* The prediction by model A is still acceptable, but model B overestimates the total force severely. In this case, model C is very accurate except for slightly overestimating the force for  $H > 0.4$  mm. The validity of circular approximation is ensured by the increased liquid volume (1.78% of effective sphere volume) of the current test.

Hence it is shown that model A can provide reasonable accuracy for liquid bridges whose volumes are small compared

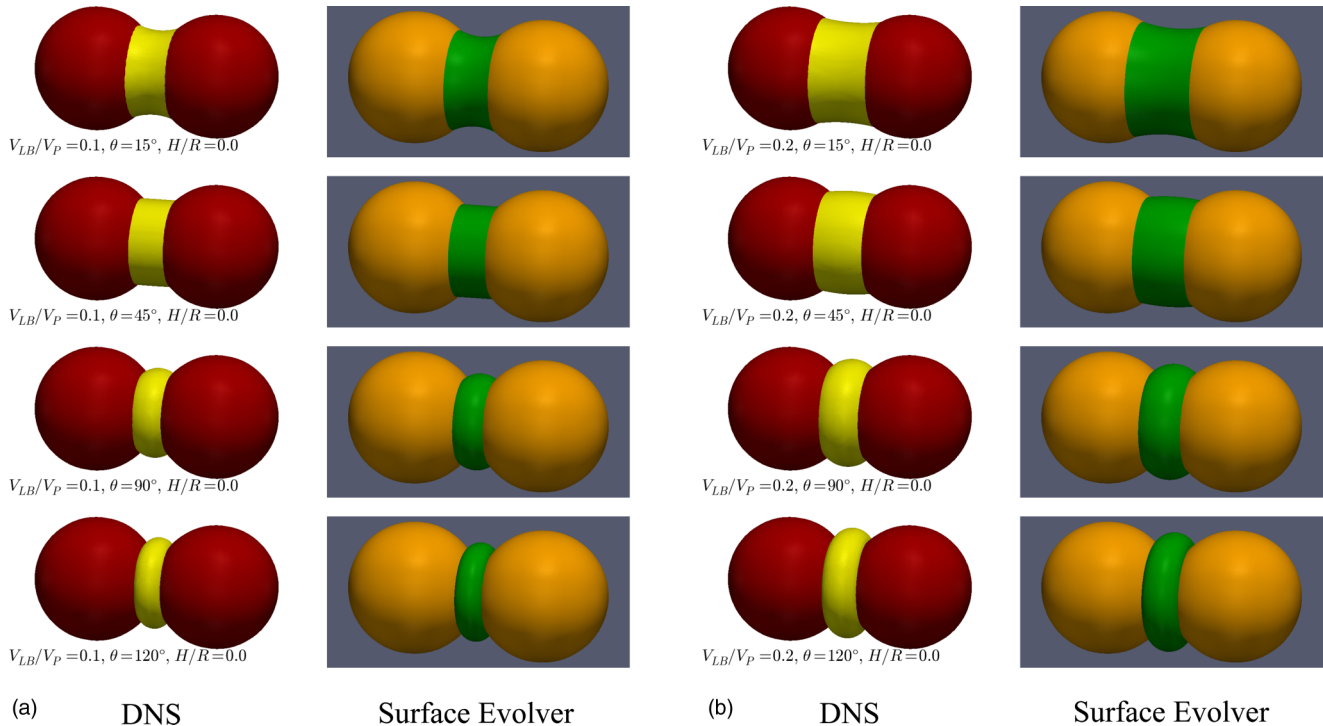


FIG. 8. Shapes for liquid bridges at zero separation distance  $H/R = 0.0$  with different volume: (a)  $V_{LB}/V_P = 0.1$  and (b)  $V_{LB}/V_P = 0.2$ . Rows from top to bottom correspond to contact angle  $\theta = 15^\circ, 45^\circ, 90^\circ$ , and  $120^\circ$ .

with the particles, although the discrepancy will be enlarged by the increasing liquid volume, contact angle, and separation distance. However, model B is incorrect because of the extra term. In fact, as Lambert *et al.* [22] commented, model A is formulated under the energetic approach, so it already includes the effects of both the tension and Laplace terms. It is thus redundant to append the extra tensile term, which has unexpectedly spoiled the results instead. Model C, the most evolved model, seems to be less accurate for very small liquid bridges, but its performance becomes notable when the liquid volume is slightly increased. The test in this section validates the DNS method in the small-volume liquid bridge regime and highlights its ability to examine model equations.

**B. Liquid bridge with relatively large volume**

Next we simulate liquid bridges with larger volumes of  $V_{LB}/V_P = 0.1$  and  $0.2$ , respectively. In the first case, the particle distance is  $H/R = 0.0, 0.1, 0.2$ , and  $0.4$ ; in the second case, the particle distance is  $H/R = 0.0, 0.2, 0.4$ , and  $0.8$ . For both cases, the contact angle is changed by  $\theta = 15^\circ, 45^\circ, 90^\circ$ , and  $120^\circ$ . Thanks to the symmetry, only half the actual bridge is computed.

We first present the comparison of the DNS results with SURFACE EVOLVER solutions at zero separation distance. Figure 8 shows the liquid bridges formed with different liquid volumes and contact angles. The results are almost visually indistinguishable. The influence of increasing contact angle is clearly seen by changing the pendular bridge (top row) to a toruslike surface (bottom row). We further give a closeup view of the meridional profile in Fig. 9 by overlaying the SURFACE EVOLVER interfaces with DNS results. From the figure, the agreement between them can also be confirmed. A small difference can be found in Fig. 9(d) where  $\theta = 120^\circ$ ; the DNS surface is slightly more retracted than that of the SURFACE EVOLVER. It may affect the evaluation of liquid bridge actions. Comparisons of bridge profiles at nonzero separations are given in Fig. 10, which shows the DNS (red curves on the right side) and the SURFACE EVOLVER (green curves on the left side) solutions for the case of liquid volume  $V_{LB}/V_P = 0.1$ . In general, they agree with each other for all combinations of separation distances and contact angles. The sectional profile is concave with the small contact angle  $\theta = 15^\circ$ . It seems to be approximately straight and parallel to the axis at  $\theta = 45^\circ$ , i.e., the liquid bridge is close to cylindrical shape. In fact, a critical embracing angle  $\alpha_c = 90^\circ - \theta$  is known for the transition between concave and convex bridge shapes

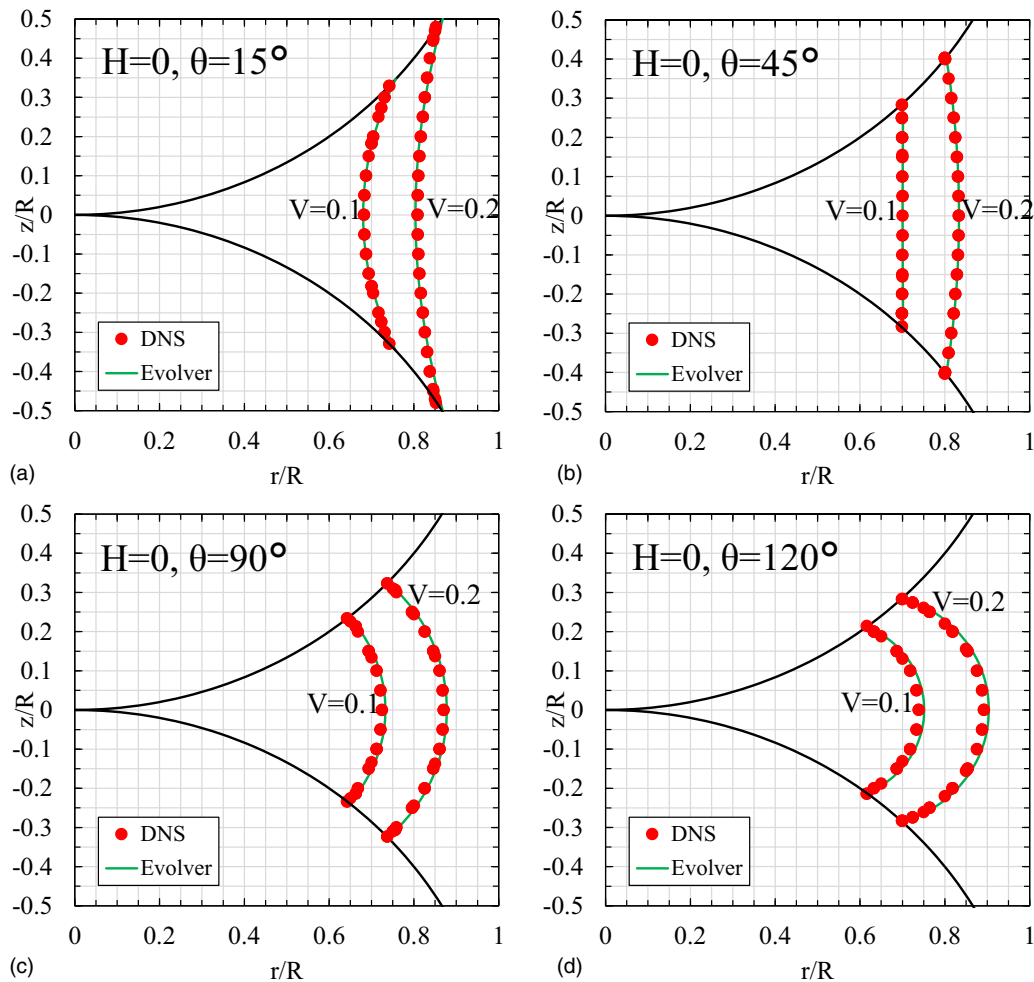


FIG. 9. Comparison of sectional profiles for liquid bridges with different contact angles and zero separation for  $V_{LB}/V_P = 0.1$  and  $0.2$ . Black lines, particle surfaces; red points, DNS results; green lines, SURFACE EVOLVER results.

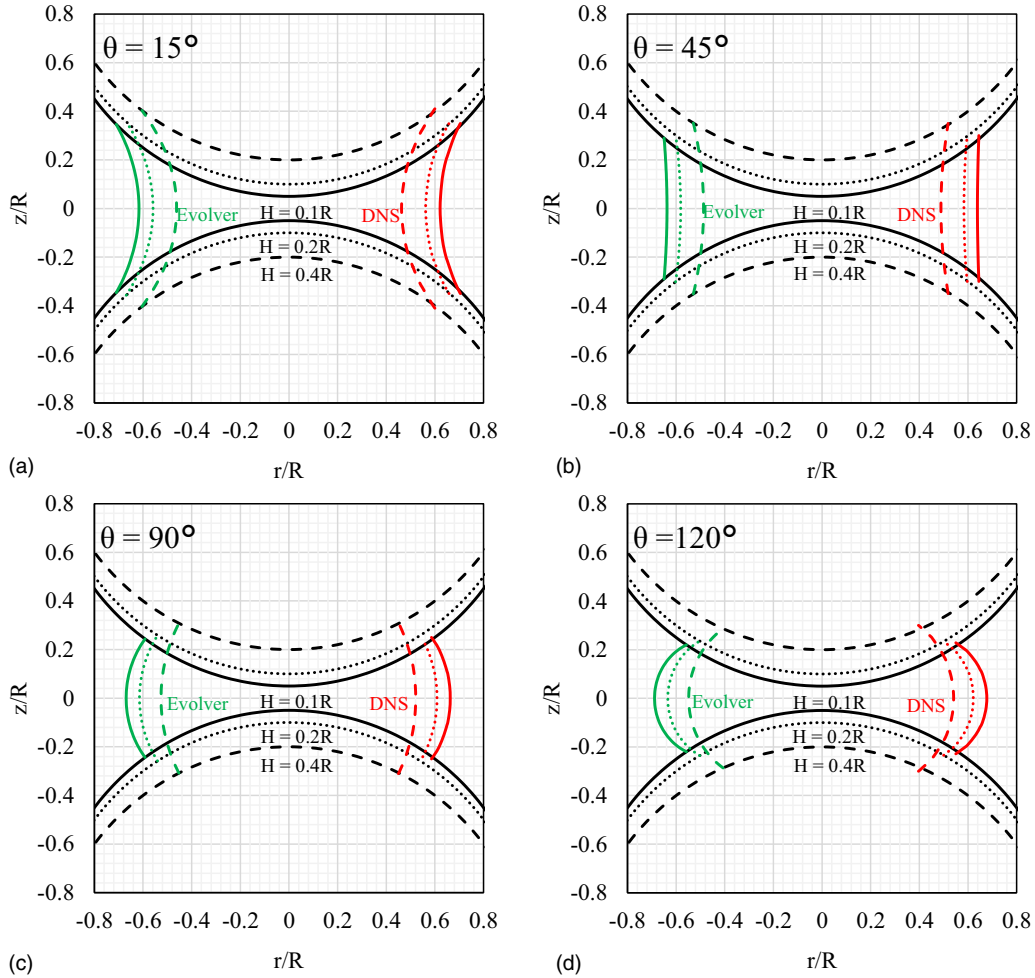


FIG. 10. Comparison of sectional profiles for liquid bridges with  $V_{LB}/V_P = 0.1$ . The lines indicate separation distances: solid lines,  $H/R = 0.1$ ; dotted lines,  $H/R = 0.2$ ; dashed lines,  $H/R = 0.4$ . The colors indicate different surfaces: black lines, particle surfaces; red lines, DNS results; green lines, SURFACE EVOLVER results.

[15], which incidentally coincides with the current  $\theta = 45^\circ$  case. Then beyond that the liquid bridge becomes convex (we emphasize that our description of bridge shape is based on whether the surface curves inward or outward in the sectional plane). Hence it is clear that the contact angle has a significant influence on the shape of the liquid bridge. Similar results have been obtained with relative volume  $V_{LB}/V_P = 0.2$ , so they are omitted here.

Figures 11(a) and 11(c) plot the total liquid bridge force obtained with the DNS, SURFACE EVOLVER, model A, and model C against the separation distance. Within the range of parameters tested, the solutions by the DNS and the SURFACE EVOLVER agree qualitatively, apart from some deviations near the zero separation for large contact angles (e.g., the line of  $\theta = 120^\circ$ ). As noted previously, in that case the simulated surface is slightly less curved than the SURFACE EVOLVER one [Fig. 9(d)], which consequently leads to a weaker action of the convex capillary bridge. This problem may be improved with further mesh refinement of the DNS. Nevertheless, the current results are still in reasonable agreement, and they qualitatively account for the influences of physical parameters. For the comparison with analytical models, model A fails to predict the liquid bridge force in all cases, despite its success

in previous tests where the liquid volume is small. For acute contact angles  $\theta = 15^\circ$  and  $45^\circ$ , the analytical model vanishes with the distance much faster than numerical results. For the neutral contact angle  $\theta = 90^\circ$ , it remains constantly zero, which is obviously wrong. For obtuse contact angles  $\theta \geq 90^\circ$ , the liquid bridge force undergoes a change of sign from being repulsive ( $F_{LB} < 0$ ) to attractive ( $F_{LB} > 0$ ). This is consistent with a previous study of a convex liquid bridge [92]. However, this transition of action cannot be recovered by model A. On the other hand, good agreements can be confirmed between the numerical results and model C, which is able to correctly describe the effects of contact angle and separation distance on static liquid bridge force with relatively large volume.

In Figs. 11(b) and 11(d), the tension term  $F_T$  and the Laplace term  $F_L$  contributing to the total liquid bridge force are plotted, which can be easily calculated from the DNS results by integration of the two terms in Eq. (21). It is emphasized that this unique advantage allows us to compute contributions from distinct interactions and thus to gain better understanding of liquid bridge problems. Unlike the DNS, it is not so natural for the SURFACE EVOLVER based on an energetic perspective to inspect different terms separately for general liquid bridges. For the simulated liquid bridges, the terms of

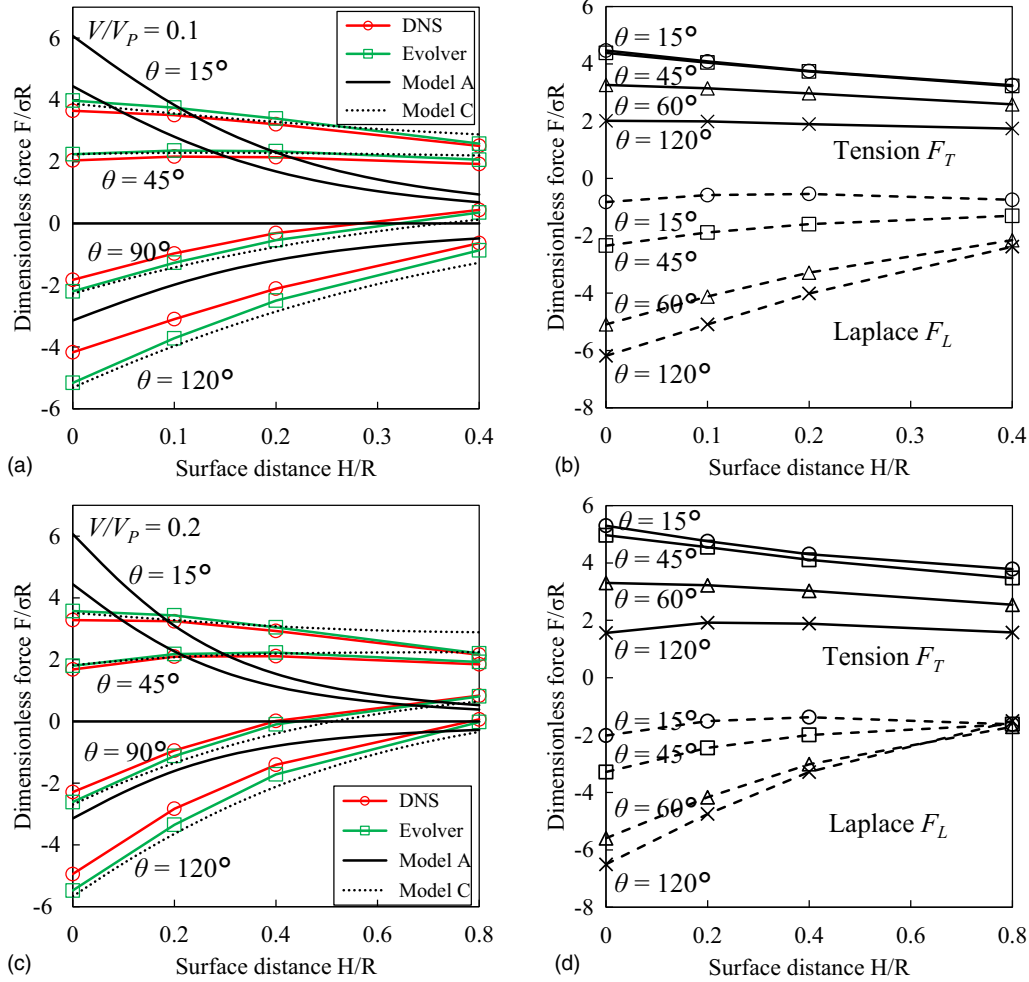


FIG. 11. Liquid bridge force vs separation distance. (a,c) Comparison of total liquid bridge force by the DNS, SURFACE EVOLVER, and analytical Models A and C. (b,d) Contributions by the tension term (solid lines) and the Laplace term (dashed lines), and the symbols are as follows: circles,  $\theta = 15^\circ$ ; squares,  $\theta = 45^\circ$ ; triangles,  $\theta = 90^\circ$ ; crosses,  $\theta = 120^\circ$ . In (a,b),  $V_{LB}/V_P = 0.1$ ; in (c,d),  $V_{LB}/V_P = 0.2$ .

tension and Laplace are comparable in strength but inverse in direction. As mentioned,  $F_T$  is always cohesive by definition. Its absolute value decreases slowly as the separation distance or the contact angle increases. Large contact angles can also cause the tension term to fall, and for some small contact angles ( $\theta = 15^\circ$  and  $45^\circ$ ) the tension forces become quite close. On the contrary,  $F_L$  arising from Laplace pressure is generally repulsive in this case. In other words, the Laplace pressure inside the liquid bridge is positive so it is pushing particles away from each other. For small contact angles ( $\theta = 15^\circ$  and  $45^\circ$ ),  $F_L$  is insensitive to the separation distance, but for large contact angles ( $\theta = 90^\circ$  and  $120^\circ$ ) it vanishes with the distance. Therefore, the net force of  $F_T$  and  $F_L$  may have different signs depending on the distance and contact angle, which explains the transition of the total force from repulsion to attraction in convex liquid bridges. This fact implies that there may exist a balance point where solid particles connected by such liquid bridges are force free. Kusumaatmaja and Lipowsky [17] calculated the equilibrium state of the liquid bridge between two parallel plates, and the current work can be helpful in extending their discussions to curved solid surfaces.

### C. Liquid bridge among multiple particles

In this section, we show numerical results for liquid bridge forces in the presence of multiple spheres. It is evident that the liquid volume must be large enough to form a bridge joining all particles in a cluster. This kind of liquid bridge can be found in the pore structures of colloidal agglomerations [43,50] and packed beds [93,94]. In the past, those “funicular” liquid bridges were calculated in two dimensions by solving the Young-Laplace equation [95] or by minimization of interfacial energy [96]. Recently, modeling of the capillary transport in three-dimensional porous media [97] via microstructures of liquid bridges and thin films covering solid surfaces has been reported [19,98]. However, the true multibody liquid bridge interactions are usually neglected or approximated by superposition of two-body actions in the literature [10,23,99,100]. Although the two-dimensional particle clusters with liquid bridges have been simulated by some authors using the phase-field method [41,43], it seems that the strength of the multibody liquid bridge is not obtained exactly, and they have not yet been calculated for three-dimensional systems. In this study, we consider the DNS of two fundamental cases involving regular structures by equal particles: the triangular

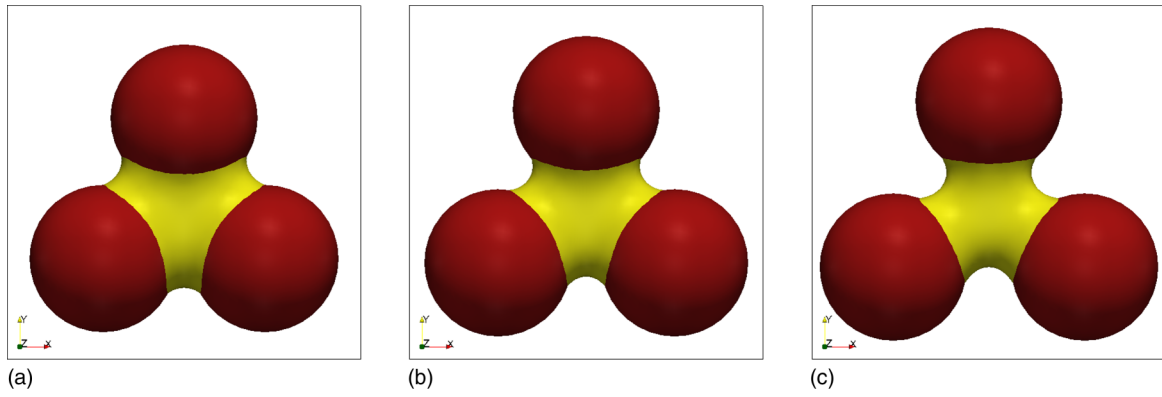


FIG. 12. Liquid bridges in triangular particle configurations at different distances: (a)  $H/R = 0.2$ , (b)  $H/R = 0.4$ , (c)  $H/R = 0.6$ .

configuration and the tetrahedral configuration, which are two of the primary cluster geometries identified in [93,94] (i.e., the “trimer” and the “tetrahedron”).

In the planar triangular configuration,  $N_p = 3$  particles with the same radius  $R$ ; the particles lie on the vertices of an equilateral triangle, for which the particle separation is defined as the distance between two adjacent sphere surfaces, or  $H = L - 2R$  with  $L$  the side length of the equilateral triangle. In our simulations, the bridge volume is  $V_{LB}/V_P = 0.26$  and the contact angle is  $\theta = 15^\circ$ . The liquid bridge force is measured for separation distance  $H/R = 0.2, 0.4$ , and  $0.6$ , respectively. Figure 12 depicts the final states of the liquid bridges. As the distance becomes longer, the liquid bridge gradually gets stretched in shape. At the largest distance  $H/R = 0.6$ , three particles are pulled aside and their connections with the liquid bridge are necked. It is confirmed that the forces exerted on three particles are almost equally pointing to the center of the triangle.

The dimensionless forces are plotted for the triangular configuration in Fig. 13(a). We note that, on calculating the liquid bridge force by the energetic approach, the geometrical relationship  $\Delta h = \Delta H/\sqrt{3}$  between the virtual displacement  $\Delta h$  and the incremental separation distance  $\Delta H$  is used.

As shown in the chart, the total liquid bridge force is adhesive and its action decays with the increasing particle distance. Qualitative agreement is found between the DNS and the SURFACE EVOLVER results. As for the individual contributions due to surface tension and pressure, it is seen that the tension term rather than the Laplace term is the major source to the total force. When the distance increases, both terms decrease. Figure 13(b) plots the interface area between liquid-gas and solid-liquid phases together with the associated energy. For the triangular liquid bridge under stretching, the area of the liquid-gas interface rises slightly, whereas the solid-liquid wetting area is torn off from the hydrophilic particle surface. As a result, the total interfacial energy rises, for which the DNS result also agrees with that of the SURFACE EVOLVER.

The tetrahedral configuration may be viewed as a part of the three-dimensional packing of particles, for which  $N_p = 4$  spheres; the spheres are placed on the vertices of a regular tetrahedron. Similarly, the separation is defined by the surface distance between two adjacent spheres; that is,  $H = L - 2R$  with  $L$  the edge length of the regular tetrahedron. Again, the volume of the liquid bridge is  $V_{LB}/V_P = 0.26$  and the contact angle is set to  $\theta = 15^\circ$ . Figure 14 depicts

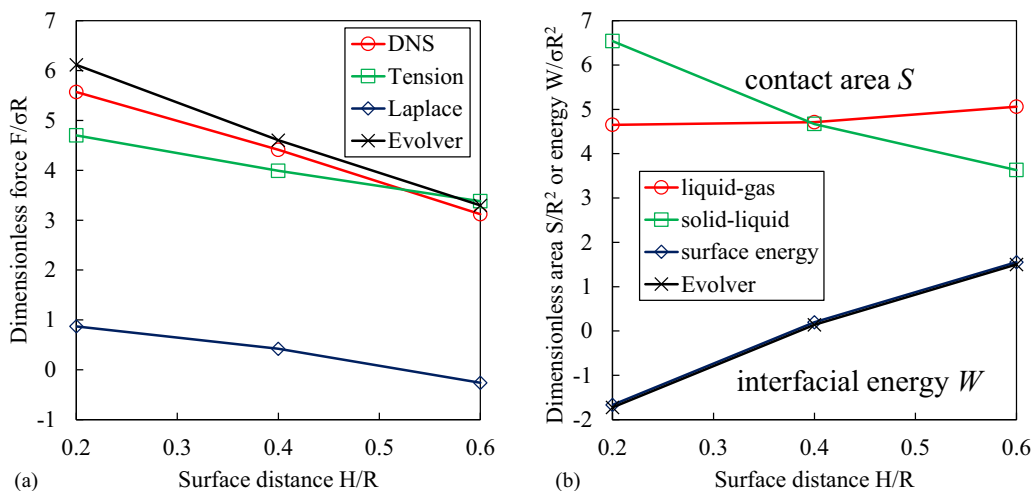


FIG. 13. Variation of liquid bridge force and energy with respect to separation distance for the triangular configuration. (a) Dimensionless force. (b) Dimensionless contact area or interfacial energy.

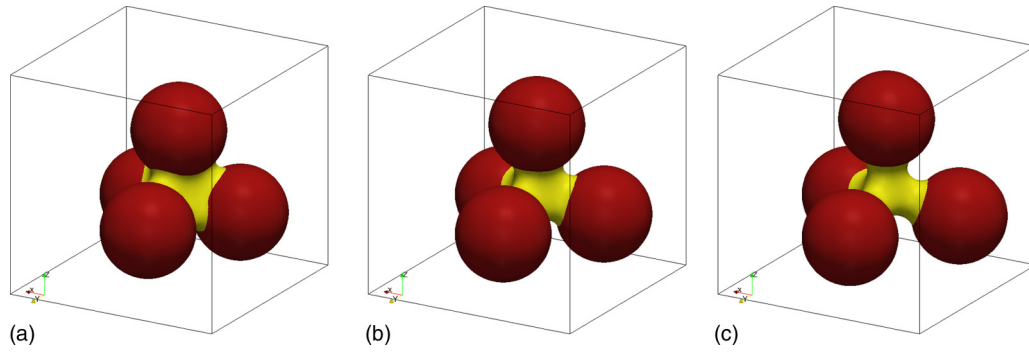


FIG. 14. Liquid bridges in tetrahedral particle configurations at different distances: (a)  $H/R = 0.2$ , (b)  $H/R = 0.4$ , (c)  $H/R = 0.6$ .

the steady bridges formed in this tetrahedral element at separation distances  $H/R = 0.2, 0.4$ , and  $0.6$ , respectively. At the smallest separation, the interstitial liquid adheres to the gap among the four spheres; when the separation is large, necking of the interface is observed.

The variation of the liquid bridge force against the separation distance is plotted for a single particle in Fig. 15(a). In this case, one has to use the relationship  $\Delta h = (\sqrt{6}/4)\Delta H$  in the energetic approach. The present trend indicates that the adhesive force loses its strength as particles move away from each other. With respect to the liquid bridge force calculated, the agreement between the DNS and SURFACE EVOLVER is noticeable. As for the composition by the tension term and the Laplace term, they are both decreasing within the range of  $H/R = 0.2$  to  $0.6$ . Unlike the triangular case, the portion of the Laplace term is now comparable to that of the tension term at a close distance  $H/R = 0.2$ , beyond which it vanishes very fast. Figure 15(b) shows the change of contact area and interfacial energy with the elongation of the tetrahedral liquid bridge. Similarly, the liquid-gas interface expands and the solid-liquid contact area shrinks. The interfacial energy calculated from the DNS is in good agreement with the reference solution by the SURFACE EVOLVER. Therefore, the complex liquid bridge among multiple particles can be conveniently modeled by using the present DNS method.

**D. Rupture of stretching liquid bridge**

In the preceding sections, the static liquid bridges between particles are computed and their interaction forces are obtained. In this part, another important aspect of liquid bridge modeling, namely, the rupture distance beyond which a steady liquid bridge cannot be formed [14], is investigated by using the DNS approach. In this problem, a liquid bridge is stretched by particles forced to move along the axial direction. The bridge structure will consequently break at some critical separation distance  $H_{Rup}$ . In this problem, two equal spheres with radius  $R = 1$  mm are aligned vertically. The lower sphere is fixed and the upper sphere moves upward with stretching velocity  $U = 0.5$  mm/s. The liquid bridge has physical properties of density  $\rho_l = 1000$  kg/m<sup>3</sup> and viscosity  $\mu_l = 0.01$  Pa s, which are larger than those of the surrounding gas phase by a factor of 100. The surface tension is  $\sigma = 0.01$  N/m and the contact angle is  $\theta = 10^\circ$ . This pendular bridge is affected by gravity  $g = 12.5$  m/s<sup>2</sup> pointing from the upper particle to the lower one. Those parameters give dimensionless numbers as follows: the Bond number  $Bo = \rho g R^2 / \sigma = 1.25$ , the Capillary number  $Ca = \mu U / \sigma = 5 \times 10^{-4}$ , and the Weber number  $We = \rho U^2 R / \sigma = 2.5 \times 10^{-5}$ , respectively. The liquid volume is varied by  $V_{LB} = 0.10, 0.15, 0.20$ , and  $0.25$  mm<sup>3</sup> to obtain corresponding rupture distances (Table II).

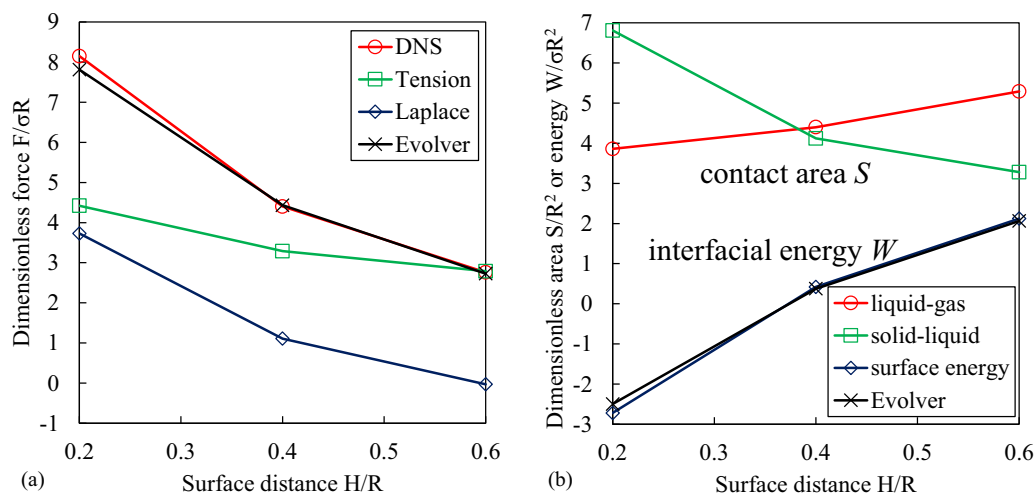


FIG. 15. Variation of liquid bridge force and energy with respect to separation distance for the tetrahedral configuration. (a) Dimensionless force. (b) Dimensionless contact area or interfacial energy.

TABLE II. Rupture of stretched liquid bridge.

Bridge volume $V/R^3$	Initial distance $H_0/R$	Rupture distance $H_{Rup}/R$
0.10	0.480	0.514
0.15	0.520	0.589
0.20	0.560	0.647
0.25	0.620	0.691

Some representative snapshots of the case  $V_{LB}/R^3 = 0.2$  are shown in Fig. 16. We can observe a smooth bridge profile at the initial stage similar to those in previous examples. When the rupture distance is reached, a thin neck is formed [Fig. 16(c)] and the bridge breaks into disconnected parts very fast. We note that such a neck is not stable and its formation mainly owes to the liquid viscosity. It is also clearly seen that the weak but finite gravitational effect causes the liquid bridge to be more biased to the lower particle, for which a larger distribution of liquid can be found after the rupture.

The critical rupture distance  $H_{Rup}$  is determined from the simulation results as the particle separation at which the axial bridge connection disappears. Figure 17 plots the liquid bridge forces acting on the upper sphere as functions of separation distance for different volumes under stretching until the breakup. The force-distance plot indicates a fast softening of the liquid bridge bond when the rupture point is approached. Series of static solutions by SURFACE EVOLVER without gravity are also presented in Fig. 17 for reference, which are obtained by iteratively increasing the particle separation until stable bridge states can no longer be found. According to Fig. 17, the rupture distance predicted by the DNS is shorter than that by the SURFACE EVOLVER as the liquid bridge volume increases. This implies that gravity has an influence on liquid bridge rupture.

The values of rupture distance are listed in Table II for each liquid bridge volume. In order to validate those results, we make a comparison with the experimental data of Mazzone *et al.* [101] and the numerical solution from [102]. We also

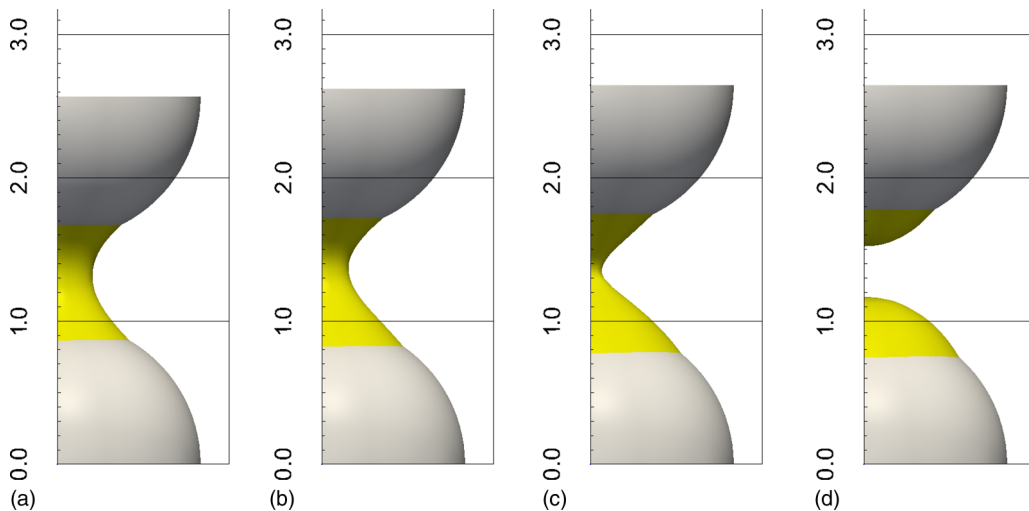


FIG. 16. Simulated liquid bridge ( $V/R^3 = 0.2$ ) under stretching at different time instants: (a)  $t = 12.5$  ms, (b)  $t = 125$  ms, (c)  $t = 170$  ms, (d)  $t = 175$  ms.

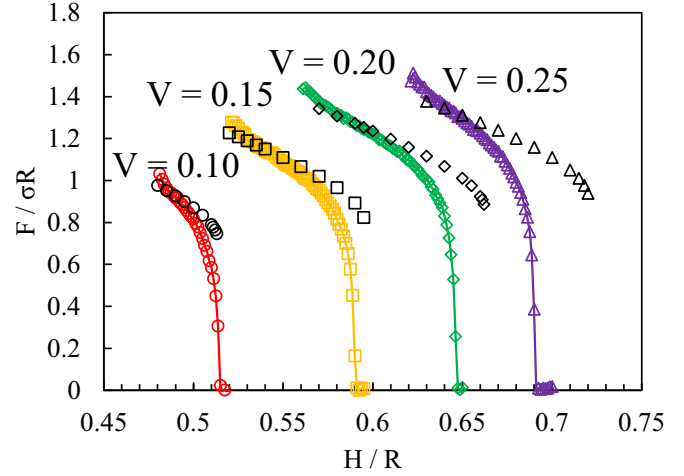


FIG. 17. Liquid bridge force on the upper particle during stretching. Colors and symbols indicate liquid volumes: red circles,  $V_{LB}/R^3 = 0.10$ ; yellow squares,  $V_{LB}/R^3 = 0.15$ ; green diamonds,  $V_{LB}/R^3 = 0.20$ ; purple triangles,  $V_{LB}/R^3 = 0.25$ . The black markers show the corresponding static solutions without gravity obtained by the SURFACE EVOLVER.

consider a widely used empirical model suggested by Lian *et al.* [14]:

$$H_{Rup} = (1 + 0.5\theta)V^{1/3}. \tag{37}$$

Another slightly different version is proposed by Willet *et al.* [24]:

$$H_{Rup} = (1 + 0.5\theta)\left(V^{1/3} + \frac{V^{2/3}}{10R}\right). \tag{38}$$

Figure 18 compares different results and correlations of  $H_{Rup}$ . It is seen that all numerical results and empirical equations tend to give longer rupture distance than the experiment of [101]. The present DNS results agree well with those of Darabi *et al.* who used boundary-fitted dynamic mesh to simulate similar problems [102]. As for empirical models

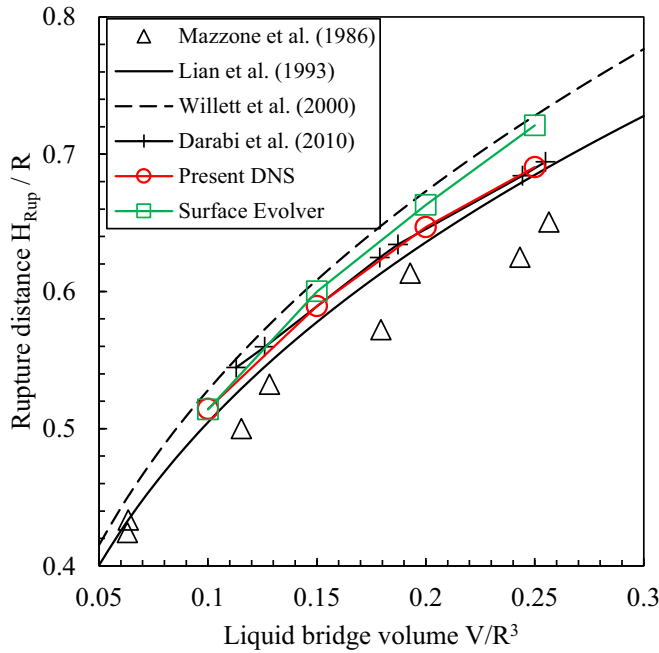


FIG. 18. Rupture distance of liquid bridge under stretching.

that do not reflect the effect of gravity, the equation of Willett *et al.* [24] overestimates the rupture distance for larger liquid volumes, which is similar to the SURFACE EVOLVER results; on the other hand, the equation of Lian *et al.* [14] coincides with the DNS results in this test. Through the current test, it is shown that the proposed method can be applied to liquid bridge rupture problems involving viscous and gravitational effects and can predict the critical rupture distance accurately.

**E. Particle motion driven by liquid bridge**

The solid particles are either fixed or forced to prescribed motion in previous simulations. In this section, we simulate the dynamic particle motions driven by the liquid bridge, which requires a full integration of capabilities to calculate the interface deformation, fluid motion, and particle displacement.

We consider a pair of particles connected by a liquid bridge which is similar to the axisymmetric problem of Villanueva *et al.* using a multicomponent phase-field method [41]. The particle radius is  $R = 1$  mm, and the solid density is  $\rho_p = 2500$  kg/m<sup>3</sup>. The liquid density is  $\rho_l = 1000$  kg/m<sup>3</sup> and the liquid viscosity is  $\mu_l = 0.01$  Pa·s; the gas density is  $\rho_g = 10$  kg/m<sup>3</sup> and the gas viscosity is  $\mu_g = 0.001$  Pa·s. The surface tension is  $\sigma = 0.01$  N/m. The liquid bridge has a relative volume of  $V_{LB}/V_p = 0.2$  with interparticle separation  $H_0 = 0.8R$ , which is initialized as a cylindrical surface connecting the particles (see Fig. 19). The particle is then released to move under the action of the liquid bridge. The spatial resolution is  $\Delta x = 0.05$  mm and the time step is  $\Delta t = 0.01$  ms. Thanks to symmetry, only half the problem domain is simulated with symmetric boundary conditions.

The behaviors during relaxation of the system toward a balanced state are studied by setting the contact angle to  $\theta = 36^\circ$  and  $90^\circ$ , respectively. For the case of  $\theta = 36^\circ$ , Fig. 20 shows some illustrative snapshots. During the first

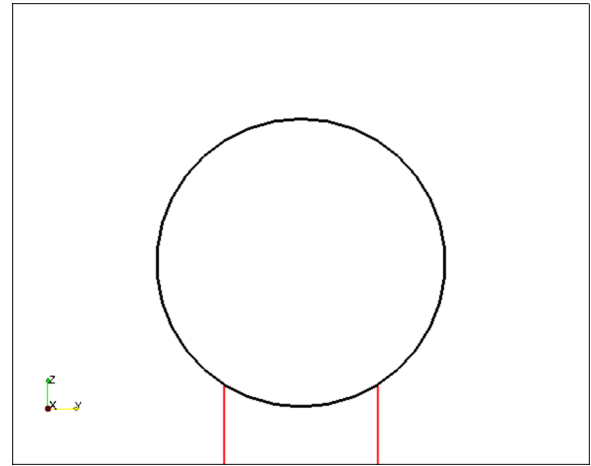


FIG. 19. Initial configuration of liquid bridge. The black bold line shows the circumference of the particle, and the red line shows the surface of the liquid bridge initialized as a cylindrical shape.

stage [Fig. 20(a)], the cylindrical shape of the bridge profile does not conform to the local contact angle condition, and hence the contact line expands to wet the particle surface. The liquid bridge then begins to pull the particle in the attractive direction [Figs. 20(b) and 20(c)]. The dynamic effect of inertia finally causes the particle to collide on the symmetry plane and rebound [Fig. 20(d)]. Such rebound arises from modeling the particle contact force by the DEM, and it may take place for several times until the kinetic energy is damped out completely, which can be confirmed from plotting temporal variations of the separation distance and the total liquid bridge force in Fig. 21(a). In Fig. 21(b), we also examined the history of the distance-force relationship. During the first approaching to the symmetry plane, it is observed that at sufficiently far distance, the total liquid bridge force is mainly composed of capillary attraction ( $F > 0$ ). Around the point  $H \sim 0.2R$ , the dynamic effect of lubrication dominates and the force switches to be repulsive ( $F < 0$ ) and reverses to the relative particle motion.

At the final state, the particle stays in contact with the symmetry plane, for which a static liquid bridge action is  $F = 2.32$  (attractive, in dimensionless units). This reasonably agrees with a reference solution of  $F_{Ref} = 2.48$  obtained by SURFACE EVOLVER at a zero-separation state (within 7% error). Their agreement confirms the fact that the liquid bridge creates a cohesive pair of particles under current conditions. On the other hand, with similar conditions of  $V_{LB}/V_p = 0.2$  and  $\theta = 36^\circ$ , Villanueva *et al.* reported a final state with nonzero separation at  $H/R = 0.21$  (see their Table 4 in [41]), which is not consistent with the attractive liquid bridge action.

For another case of  $\theta = 90^\circ$ , as discussed previously, the bridge profile is convex so there may exist a balanced point at  $H > 0$  at which the liquid bridge force becomes zero. Representative snapshots are shown in Fig. 22 to understand this behavior. In Fig. 22(a), the bridge is recovering from the initial cylindrical shape, and the difference from the previous case is a receding contact line. Again the liquid bridge attracts the particle moving toward the symmetry plane [Fig. 22(b)]. However, the liquid bridge can effectively prevent the particle collision in this case. In Fig. 22(c) it almost reaches the state of

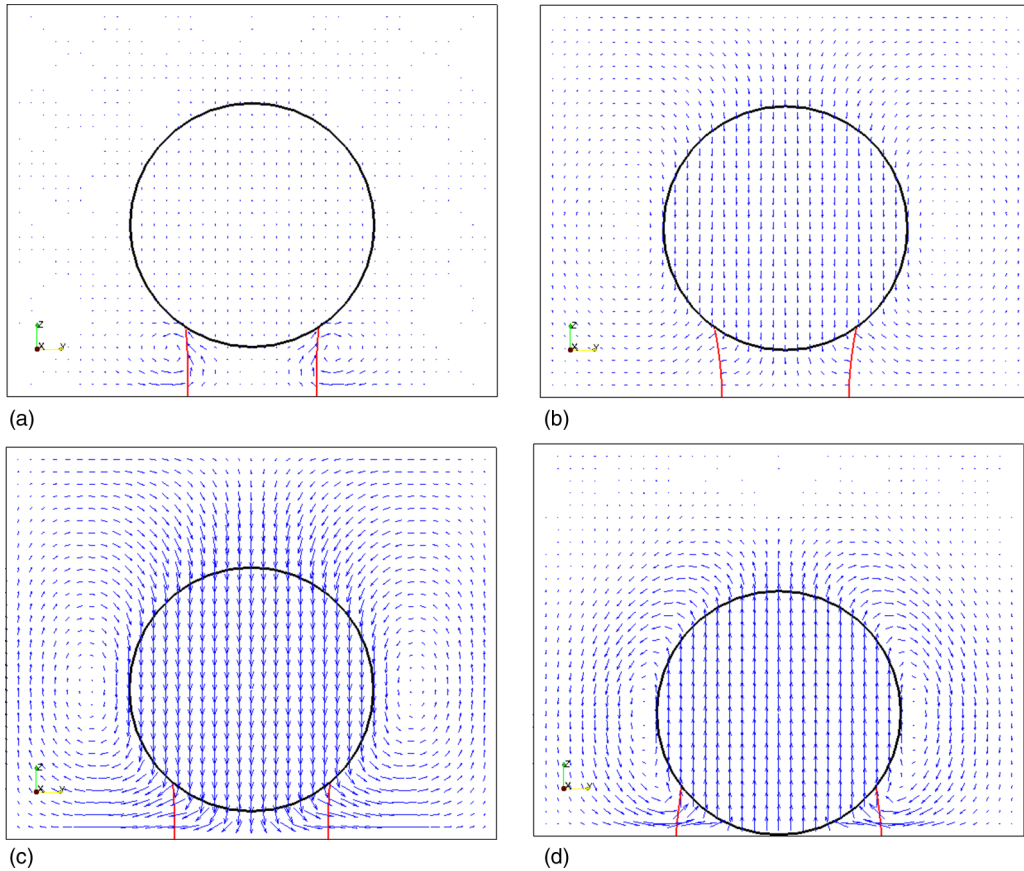


FIG. 20. Temporal evolution of particle connected by liquid bridge with contact angle  $\theta = 36^\circ$ . The velocity profiles (blue arrows) are shown for different configurations of the particle position (black circles) and liquid bridge shape (red line). (a)  $t = 1$  ms, initial wetting. (b)  $t = 5$  ms, particle acceleration under attraction. (c)  $t = 15$  ms, approaching the symmetry plane. (d)  $t = 24$  ms, just after the first rebound.

maximum compression, and in Fig. 22(d) the particle moves in the repulsive direction. The temporal variations of separation distance and liquid bridge force of Fig. 23(a) imply that the oscillatory behavior is similar to a spring system with damping. According to the distance-force plot of Fig. 23(b), it finally converges to a balanced state where  $F = 0$  and  $H > 0$ .

After performing the simulation with sufficiently long time, we find that the particle finally stops at a separation distance of  $H/R = 0.40$ . Using SURFACE EVOLVER, the balanced point for  $F = 0$  is obtained around  $H_{Ref} = 0.42R$ , which agrees well

with the current result (below 5% error). This agreement is remarkable in comparison with the past result of  $H = 0.68$  (see Table 4 of Villanueva *et al.* [41]), although the exact reason of their deviation is not clear. On the other hand, the present DNS method can satisfactorily compute the solid particle dynamics driven by the liquid bridge and correctly predict the state of equilibrium. Besides that, another advantage of the present DNS is the easy calculation of total liquid bridge force for individual particles, which cannot be achieved by using the method of [41].

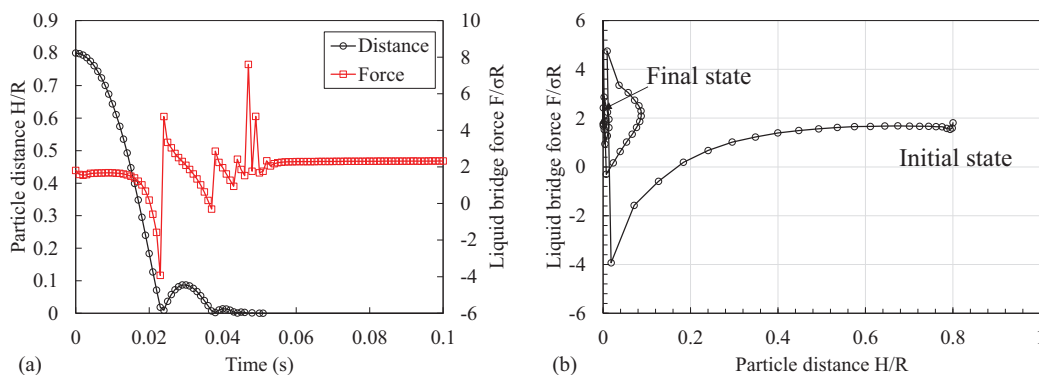


FIG. 21. Plot of particle distance and liquid bridge force for  $\theta = 36^\circ$ . (a) Plot against time. (b) Distance-force plot.

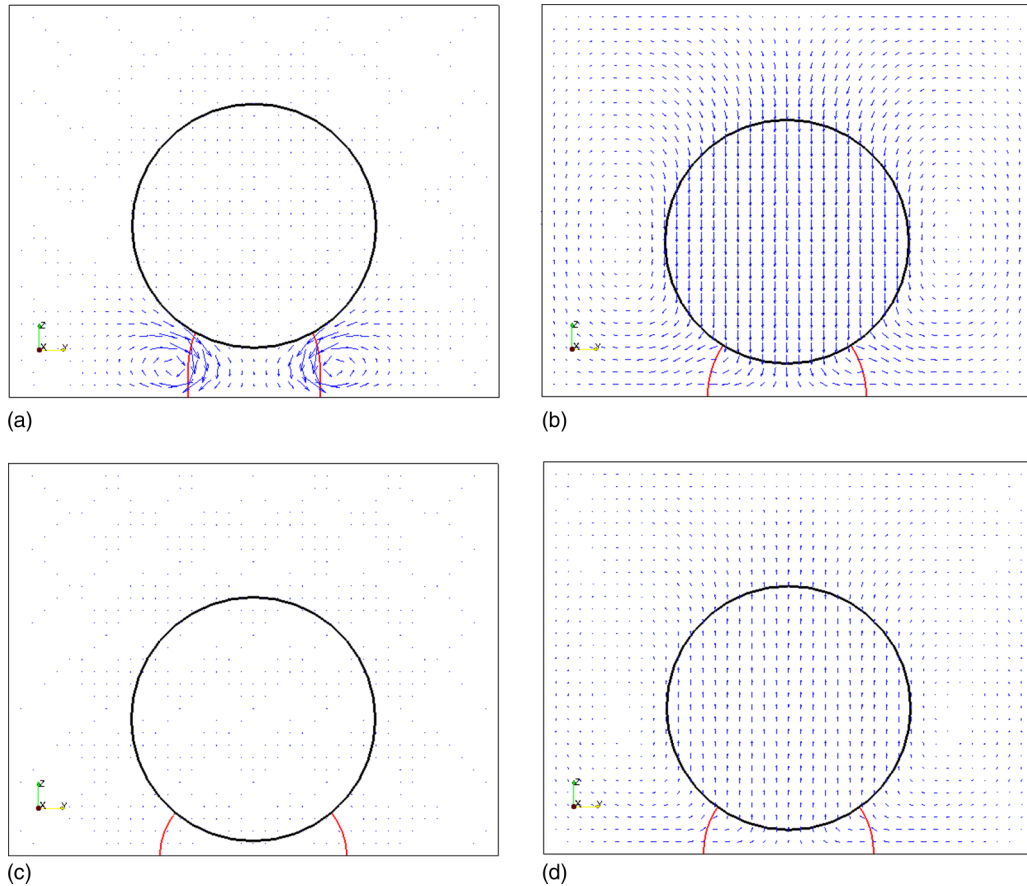


FIG. 22. Temporal evolution of particle connected by liquid bridge with contact angle  $\theta = 90^\circ$ . The velocity profiles (blue arrows) are shown for different configurations of the particle position (black circles) and liquid bridge shape (red line). (a)  $t = 1$  ms, initial wetting. (b)  $t = 20$  ms, undergoing attraction. (c)  $t = 40$  ms, the bridge is now near its maximum compression. (d)  $t = 60$  ms, receding under repulsion.

**VII. CONCLUSIONS**

In this study, the VOF-IB-DNS method is developed for simulating three-dimensional gas-solid-liquid flows involving capillary interactions. It uses the VOF method to track the fluid interface and solves the incompressible Navier-Stokes equations for multiphase flows. Solid particles are modeled by the IB method which is modified to calculate the fluid-particle interactions in three-phase flow systems. The proposed method can simulate complex gas-solid-liquid flow problems with ease. As a DNS method, its ability to calculate the

hydrodynamic and capillary forces *a priori* has enabled an alternative approach to examine and establish model equations for three-phase interactions.

The main subject of this paper is the numerical study of liquid bridges among spherical particles by using the VOF-IB-DNS method. The purpose is twofold: to validate our DNS method by qualitative comparison with available analytical and numerical solutions, and to investigate the liquid bridge forces in a range of parameters that have not been thoroughly studied in the past. First we examine the static interaction force in the context of small-volume liquid bridges, and then

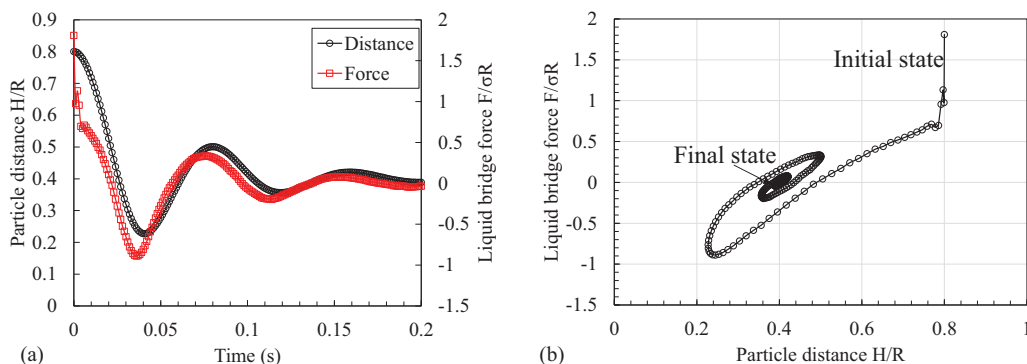


FIG. 23. Plot of particle distance and liquid bridge force for  $\theta = 90^\circ$ . (a) Plot against time. (b) Distance-force plot.

those associated with larger liquid volumes. Simulations are carried out by varying the parameters of bridge volume, contact angle, and separation distance to inspect their influences. The DNS results of static liquid bridge force are validated against the reference solution by SURFACE EVOLVER, and they are compared with different types of analytical models to check the applicability in a wide range of flow cases. We also present results for liquid bridges among multiple spheres. Particles arranged regularly in triangular and tetrahedral structures are computed, for which the multibody liquid bridge forces are obtained. Next the breakup of the liquid bridge caused by axial stretching of end particles is simulated. The effects of viscosity and gravity on bridge shape before rupture and liquid distribution after rupture are satisfactorily reflected by the DNS results. The critical rupture distances predicted by the DNS are also in good agreement with reference data. In another test, the DNS calculates the particle motion driven by relaxing the liquid bridge, which is a typically dynamic problem involving fully coupled dynamics of interface, fluid, and solid. The dynamic interactions are obtained showing attractive or repulsive actions depending on the contact angle and particle motion. In comparison with a past study, the present method can also yield balanced states that are more consistent with analysis of force balance, which is considered to be proof of better resolving the physics in gas-solid-liquid flows.

Therefore, the numerical studies in this work justify the VOF-IB-DNS method in several important aspects of bond force, rupture distance, dynamic motion, and clustered state with successful prediction of the liquid bridge physics. Especially owing to its capability to obtain liquid bridge behavior and interaction directly, this method might be helpful for developing more general models of wet granular materials. It can also be suitable for simulating other gas-solid-liquid flows where the particle-interface interaction is important.

In the future, we are planning to perform detailed investigations of complex liquid bridges in multiple particle configurations. Besides that, the current algorithm will be enhanced by our arbitrary shape boundary model [68] so the liquid bridge interaction between nonspherical particles could be evaluated. Another research topic is the fully resolved DNS for dynamic liquid bridges involving particle motion, bridge rupture, and liquid redistribution, for which a computational model of contact angle hysteresis is to be incorporated.

#### ACKNOWLEDGMENT

This study is supported by the Japan Society for the Promotion of Science and the Ricoh Company Ltd.

- 
- [1] C. W. Extrand and S. I. Moon, *Langmuir* **25**, 6239 (2009).
  - [2] J. N. Israelachvili, *Intermolecular and Surface Forces*, 3rd ed. (Academic Press, Waltham, MA, 2010).
  - [3] Y. I. Rabinovich, M. S. Esayanur, and B. M. Moudgil, *Langmuir* **21**, 10992 (2005).
  - [4] L. Yang, Y. Tu, and H. Fang, *Soft Matter* **6**, 6178 (2010).
  - [5] S. Ulrich, T. Aspelmeier, A. Zippelius, K. Roeller, A. Fingerle, and S. Herminghaus, *Phys. Rev. E* **80**, 031306 (2009).
  - [6] V. Richefeu, M. S. El Youssofi, and F. Radjaï, *Phys. Rev. E* **73**, 051304 (2006).
  - [7] T. Mikami, H. Kamiya, and M. Horio, *Chem. Eng. Sci.* **53**, 1927 (1998).
  - [8] R. Zhu, S. Li, and Q. Yao, *Phys. Rev. E* **87**, 022206 (2013).
  - [9] P. Y. Liu, R. Y. Yang, and A. B. Yu, *Phys. Fluids* **23**, 13304 (2011).
  - [10] Y. Tsunazawa, D. Fujihashi, S. Fukui, M. Sakai, and C. Tokoro, *Adv. Powder Technol.* **27**, 652 (2016).
  - [11] X. Sun and M. Sakai, *Chem. Eng. Sci.* **134**, 531 (2015).
  - [12] M. A. Erle, D. C. Dyson, and N. R. Morrow, *AIChE J.* **17**, 115 (1971).
  - [13] F. R. De Bisschop and W. J. Rigole, *J. Colloid Interface Sci.* **88**, 117 (1982).
  - [14] G. Lian, C. Thornton, and M. J. Adams, *J. Colloid Interface Sci.* **161**, 138 (1993).
  - [15] D. Megias-Alguacil and L. J. Gauckler, *AIChE J.* **55**, 1103 (2009).
  - [16] Y. Wang, S. Michielsen, and H. J. Lee, *Langmuir* **29**, 11028 (2013).
  - [17] H. Kusumaatmaja and R. Lipowsky, *Langmuir* **26**, 18734 (2010).
  - [18] R. de Ruiter, C. Semprebon, M. van Gorcum, M. H. G. Duits, M. Brinkmann, and F. Mugele, *Phys. Rev. Lett.* **114**, 234501 (2015).
  - [19] R. Mani, C. Semprebon, D. Kadau, H. J. Herrmann, M. Brinkmann, and S. Herminghaus, *Phys. Rev. E* **91**, 042204 (2015).
  - [20] Y. I. Rabinovich, M. S. Esayanur, K. D. Johanson, J. J. Adler, and B. M. Moudgil, *J. Adhes. Sci. Technol.* **16**, 887 (2002).
  - [21] P. Lambert and A. Delchambre, *Langmuir* **21**, 9537 (2005).
  - [22] P. Lambert, A. Chau, A. Delchambre, and S. Régnier, *Langmuir* **24**, 3157 (2008).
  - [23] S. Radl, E. Kalvoda, B. J. Glasser, and J. G. Khinast, *Powder Technol.* **200**, 171 (2010).
  - [24] C. D. Willett, M. J. Adams, S. A. Johnson, and J. P. K. Seville, *Langmuir* **16**, 9396 (2000).
  - [25] W. Huppmann and H. Riegger, *Acta Metall.* **23**, 965 (1975).
  - [26] R. B. Heady and J. W. Cahn, *Metall. Trans.* **1**, 185 (1970).
  - [27] Y. Chen, Y. Zhao, H. Gao, and J. Zheng, *Particuology* **9**, 374 (2011).
  - [28] A. F. Payam and M. Fathipour, *Particuology* **9**, 381 (2011).
  - [29] L.-F. Wang, W.-B. Rong, L.-N. Sun, L.-G. Chen, and B. Shao, *Chin. Phys. Lett.* **26**, 126801 (2009).
  - [30] K. A. Brakke, *Exp. Math.* **1**, 141 (1992).
  - [31] A. Virozub, N. Haimovich, and S. Brandon, *Langmuir* **25**, 12837 (2009).
  - [32] T. P. Farmer and J. C. Bird, *J. Colloid Interface Sci.* **454**, 192 (2015).

- [33] R. Ardito, A. Corigliano, A. Frangi, and F. Rizzini, *Eur. J. Mech., A: Solids* **47**, 298 (2014).
- [34] A. Takei, K. Matsumoto, and I. Shimoyama, *Langmuir* **26**, 2497 (2010).
- [35] D. J. Broesch and J. Frechette, *Langmuir* **28**, 15548 (2012).
- [36] S. Dasgupta, M. Katava, M. Faraj, T. Auth, and G. Gompper, *Langmuir* **30**, 11873 (2014).
- [37] A. S. Joshi and Y. Sun, *Phys. Rev. E* **79**, 066703 (2009).
- [38] K. W. Connington, T. Lee, and J. F. Morris, *J. Comput. Phys.* **283**, 453 (2015).
- [39] P. Singh and D. D. Joseph, *J. Fluid Mech.* **530**, 31 (2005).
- [40] J. Zhuang and Y. S. Ju, *Langmuir* **31**, 10173 (2015).
- [41] W. Villanueva, K. Grönhagen, G. Amberg, and J. Ågren, *Comput. Mater. Sci.* **47**, 512 (2009).
- [42] P. C. Millett and Y. U. Wang, *J. Colloid Interface Sci.* **353**, 46 (2011).
- [43] T.-L. Cheng and Y. U. Wang, *Langmuir* **28**, 2696 (2012).
- [44] M. Fujita, O. Koike, and Y. Yamaguchi, *J. Comput. Phys.* **281**, 421 (2015).
- [45] H. Kan, H. Nakamura, and S. Watano, *Chem. Eng. Sci.* **138**, 607 (2015).
- [46] K. Yokoi, *J. Comput. Phys.* **226**, 1985 (2007).
- [47] T. Kajishima, S. Takiguchi, H. Hamasaki, and Y. Miyake, *JSME Int. J., Ser. B* **44**, 526 (2001).
- [48] T. Kajishima and S. Takiguchi, *Int. J. Heat Fluid Flow* **23**, 639 (2002).
- [49] M. Sussman, in *Adaptive Method of Lines*, edited by A. Vande Wouwer, P. Saucez, and W. Schiesser (Chapman and Hall/CRC, Boca Raton, FL, 2001).
- [50] I. U. Vakarelski, J. W. Kwek, X. Tang, S. J. O'Shea, and D. Y. C. Chan, *Langmuir* **25**, 13311 (2009).
- [51] X. Sun and M. Sakai, *Chem. Eng. Sci.* **139**, 221 (2016).
- [52] B. Bunner and G. Tryggvason, *J. Fluid Mech.* **466**, 17 (2002).
- [53] S. Afkhami, S. Zaleski, and M. Bussmann, *J. Comput. Phys.* **228**, 5370 (2009).
- [54] R. G. Cox, *J. Fluid Mech.* **168**, 169 (1986).
- [55] K. Yokoi, D. Vadillo, J. Hinch, and I. Hutchings, *Phys. Fluids* **21**, 72102 (2009).
- [56] L. H. Tanner, *J. Phys. D: Appl. Phys.* **12**, 1473 (2001).
- [57] M. Griebel and M. Klitz, in *Singular Phenomena and Scaling in Mathematical Models*, edited by M. Griebel (Springer International Publishing, Cham, Switzerland, 2014), pp. 297–325.
- [58] Y. D. Shikhmurzaev, *Capillary Flows with Forming Interfaces* (Chapman & Hall/CRC, Boca Raton, FL, 2008).
- [59] D. Legendre and M. Maglio, *Comput. Fluids* **113**, 2 (2015).
- [60] J. Yang and F. Stern, *J. Comput. Phys.* **228**, 6590 (2009).
- [61] K. Yokoi, *J. Comput. Phys.* **232**, 252 (2013).
- [62] M. Arienti and M. Sussman, *Int. J. Multiphase Flow* **59**, 1 (2014).
- [63] H.-R. Liu and H. Ding, *J. Comput. Phys.* **294**, 484 (2015).
- [64] M. Lepilliez, E. R. Popescu, F. Gibou, and S. Tanguy, *J. Comput. Phys.* **321**, 1217 (2016).
- [65] M. M. Francois, S. J. Cummins, E. D. Dendy, D. B. Kothe, J. M. Sicilian, and M. W. Williams, *J. Comput. Phys.* **213**, 141 (2006).
- [66] B. Lafaurie, C. Nardone, R. Scardovelli, S. Zaleski, and G. Zanetti, *J. Comput. Phys.* **113**, 134 (1994).
- [67] P. A. Cundall and O. D. L. Strack, *Géotechnique* **29**, 47 (1979).
- [68] Y. Shigeto and M. Sakai, *Chem. Eng. J.* **231**, 464 (2013).
- [69] X. Sun, M. Sakai, M.-T. Sakai, and Y. Yamada, *Chem. Eng. J.* **246**, 122 (2014).
- [70] R. Glowinski, T.-W. Pan, T. I. Hesla, and D. D. Joseph, *Int. J. Multiphase Flow* **25**, 755 (1999).
- [71] A. S. Joshi and Y. Sun, *Phys. Rev. E* **82**, 041401 (2010).
- [72] S.-Y. Lin, Y.-H. Chin, J.-J. Hu, and Y.-C. Chen, *Int. J. Numer. Methods Fluids* **67**, 1771 (2011).
- [73] R. Seto, R. Mari, J. F. Morris, and M. M. Denn, *Phys. Rev. Lett.* **111**, 218301 (2013).
- [74] S. Gallier, E. Lemaire, L. Lobry, and F. Peters, *J. Comput. Phys.* **256**, 367 (2014).
- [75] S. Gallier, E. Lemaire, F. Peters, and L. Lobry, *J. Fluid Mech.* **757**, 514 (2014).
- [76] H. Shinto, D. Komiyama, and K. Higashitani, *Langmuir* **22**, 2058 (2006).
- [77] J. Onishi, A. Kawasaki, Y. Chen, and H. Ohashi, *Comput. Math. Appl.* **55**, 1541 (2008).
- [78] G. Liang, Z. Zeng, Y. Chen, J. Onishi, H. Ohashi, and S. Chen, *J. Comput. Phys.* **248**, 323 (2013).
- [79] G. B. Davies, T. Krüger, P. V. Coveney, and J. Harting, *J. Chem. Phys.* **141**, 154902 (2014).
- [80] G. B. Davies, T. Krüger, P. V. Coveney, J. Harting, and F. Bresme, *Adv. Mater.* **26**, 6715 (2014).
- [81] Q. Xie, G. B. Davies, F. Günther, and J. Harting, *Soft Matter* **11**, 3581 (2015).
- [82] S. Bogner and U. Rüde, *Comput. Math. Appl.* **65**, 901 (2013).
- [83] K. W. Connington, M. Z. Miskin, T. Lee, H. M. Jaeger, and J. F. Morris, *Int. J. Multiphase Flow* **76**, 32 (2015).
- [84] P. Singh, D. D. Joseph, S. K. Gurupatham, B. Dalal, and S. Nudurupati, *Proc. Natl. Acad. Sci. U. S. A.* **106**, 19761 (2009).
- [85] M. Fujita, O. Koike, and Y. Yamaguchi, *Appl. Phys. Express* **6**, 36501 (2013).
- [86] K. Washino, H. S. Tan, A. D. Salman, and M. J. Hounslow, *Powder Technol.* **206**, 161 (2011).
- [87] K. Washino, H. S. Tan, M. J. Hounslow, and A. D. Salman, *Chem. Eng. Sci.* **93**, 197 (2013).
- [88] O. Pitois, P. Moucheron, and X. Chateau, *J. Colloid Interface Sci.* **231**, 26 (2000).
- [89] P. Gopalkrishnan, I. Manas-Zloczower, and D. L. Feke, *Adv. Powder Technol.* **19**, 277 (2008).
- [90] S. Mitra, M. J. Sathe, E. Doroodchi, R. Utikar, M. K. Shah, V. Pareek, J. B. Joshi, and G. M. Evans, *Chem. Eng. Sci.* **100**, 105 (2013).
- [91] A. Chau, S. Rignier, A. Delchambre, and P. Lambert, *Model. Simul. Mater. Sci. Eng.* **15**, 305 (2007).
- [92] D. Megias-Alguacil and L. J. Gauckler, *Powder Technol.* **198**, 211 (2010).
- [93] M. Scheel, R. Seemann, M. Brinkmann, M. Di Michiel, A. Sheppard, B. Breidenbach, and S. Herminghaus, *Nat. Mater.* **7**, 189 (2008).
- [94] M. Scheel, R. Seemann, M. Brinkmann, M. Di Michiel, A. Sheppard, and S. Herminghaus, *J. Phys.: Condens. Matter* **20**, 494236 (2008).
- [95] M. E. D. Urso, C. J. C. J. Lawrence, and M. J. Adams, *Chem. Eng. Sci.* **57**, 677 (2002).

- [96] Z. Grof, C. J. Lawrence, and F. Štěpánek, *J. Colloid Interface Sci.* **319**, 182 (2008).
- [97] A. V. Lukyanov, M. M. Sushchikh, M. J. Baines, and T. G. Theofanous, *Phys. Rev. Lett.* **109**, 214501 (2012).
- [98] K. Melnikov, R. Mani, F. K. Wittel, M. Thielmann, and H. J. Herrmann, *Phys. Rev. E* **92**, 022206 (2015).
- [99] N. Mitarai and H. Nakanishi, *EPL* **88**, 64001 (2009).
- [100] N. Mitarai and H. Nakanishi, *AIP Conf. Proc.* **1227**, 214 (2010).
- [101] D. N. Mazzone, G. I. Tardos, and R. Pfeffer, *J. Colloid Interface Sci.* **113**, 544 (1986).
- [102] P. Darabi, T. Li, K. Pougatch, M. Salcudean, and D. Grecov, *Chem. Eng. Sci.* **65**, 4472 (2010).